

Pre-collapse motion of the February 2021 Chamoli rock-ice avalanche, Indian Himalaya

Maximillian Van Wyk de Vries^{1,2,3}, Shashank Bhushan⁴, Mylène Jacquemart^{5,6}, César Deschamps-Berger⁷, Etienne Berthier⁸, Simon Gascoin⁷, David E. Shean⁴, Dan H. Shugar⁹, and Andreas Kääh¹⁰

¹St Anthonys Falls laboratory, University of Minnesota, Minneapolis, MN, USA

²Department of Earth and Environmental Sciences, University of Minnesota, Minneapolis, MN, USA

³School of Environmental Sciences, University of Liverpool, Liverpool, L3 5DA, UK.

⁴Department of Civil and Environmental Engineering, University of Washington, Seattle, WA, USA

⁵Laboratory for Hydraulics, Hydrology, and Glaciology (VAW), ETH Zurich, Zurich, Switzerland

⁶Swiss Federal Institute for Forest, Snow, and Landscape Research (WSL), Birmensdorf, Switzerland

⁷CESBIO, Université de Toulouse, CNRS, CNES, IRD, INRAE, UPS, Toulouse, France

⁸LEGOS, Université de Toulouse, CNES, CNRS, IRD, UPS, Toulouse, France

⁹Water, Sediment, Hazards, and Earth-surface Dynamics (waterSHED) Lab, Department of Geoscience, University of Calgary, Canada

¹⁰Department of Geosciences, University of Oslo, Oslo, Norway

Correspondence: Maximillian Van Wyk de Vries (vanwy048@umn.edu)

Abstract. ~~On~~ Landslides are a major geohazard that cause thousands of fatalities every year. Despite their importance, identifying unstable slopes and forecasting collapses remains a major challenge. In this study, we use the 7th of February 2021, a large Chamoli rock-ice avalanche triggered a debris flow in Chamoli district, Uttarakhand, India, leaving over 200 dead or missing. The rock-ice avalanche originated from a steep, glacierized north-facing slope. In this work, we as a data-rich
5 example to investigate the potential of remotely-sensed datasets for the assessment of slope stability. We investigate imagery over the three decades preceding collapse and assess the precursory signs exhibited by this slope prior to the catastrophic collapse. We evaluate monthly slope motion from 2015 to 2021 through feature tracking of high-resolution optical satellite imagery. We then combine these data with a time series of pre- and post-event DEMs, which we use to evaluate elevation change
10 over the same area. Both datasets show that the 26.9 Mm³ collapse block moved over 10 m horizontally and vertically in the five years preceding collapse, with particularly rapid motion occurring in the summers of 2017 and 2018. We propose that the collapse results from a combination of snow-loading in a deep headwall crack and permafrost degradation in the heavily jointed bedrock. ~~Our observation of~~ Despite observing a clear precursory signal ~~highlights the potential of satellite imagery for monitoring the stability of high-risk slopes. We find, we find find~~
15 that the timing of the Chamoli rock-ice avalanche could likely not have been forecast from satellite data alone. Our results highlight the potential of remotely-sensed imagery for assessing landslide hazard in remote areas, but that challenges remain for operational hazard monitoring.

1 Introduction

1.1 Landslide hazard

Landslides ~~represent are~~ a major geohazard, ~~and that~~ cause thousands of deaths each year (Petley, 2012; Froude and Petley, 2018). ~~Preventing or mitigating~~ Mitigating landslide hazard is a major challenge facing geoscientists and hazard managers.

20 Evaluating landslide hazard is challenging due to the wide range of source conditions and the varying temporal scales at which the driving processes interact. Landslides are also associated with a wide range of short- to long-term triggers, ranging from earthquakes to water flow, or simple weaknesses in the rock, which further complicates their forecasting and process understanding (van Westen et al., 2006).

Ground-based observations of displacement (e.g. with GNSS/GPS, ground-based radar interferometry), tilt (e.g. inclinometers), pressure (e.g. piezometers), and other parameters-variables can be useful in monitoring landslide progression (e.g. Uhlemann et al., 2016). When observed, landslide precursory signs may be used to forecast a failure time or improve monitoring (Federico et al., 2012; Fukuzono, 1985; Intrieri et al., 2019; Wegmann et al., 2003). In many cases the nature and magnitude of these precursory signs precludes their detection in the absence of sensitive equipment. In-situ observations can be sensitive to even small changes in slope properties, and are therefore valuable for the forecasting of instability forecasting a destabilization
30 (Sättele et al., 2015; Stähli et al., 2015). However, ground-based observations have important limitations: (i) Prior knowledge of a potential slope instability is required in order for the correct instrumentation to be installed in the right locations, (ii) the landslide source regions may be located in inaccessible terrain region may be inaccessible, preventing the installation of in-situ monitoring equipment, (iii) monitoring systems can be prohibitively expensive and require highly specialized expertise for data evaluation, and (iv) the area that can be monitored is generally limited to individual hillslopes. Altogether, ground-based
35 monitoring techniques are useful for landslide monitoring in many cases, but are insufficient for monitoring large regions or where a-priori knowledge is lacking.

An increase in satellite data availability and resolution has promoted remote sensing as an alternative or complementary landslide detection and monitoring tool (e.g. Kirschbaum et al., 2019; Dille et al., 2021). Satellite remote sensing may lack the precision of some ground-based monitoring techniques, but but it can provide a low-cost (for the end user) and
40 easily accessible way to monitor vast and inaccessible terrain at daily to weekly temporal and 0.3 to 30 m revisit times and 0.3 m to 30 m spatial resolution. Qualitative visual analysis of satellite imagery allows for the rapid identification of surface changes that may be associated with slope instabilities or the initiation of landslide motion. Further quantitative processing of satellite imagery enables the monitoring of horizontal and vertical land motions – for example via feature tracking or stereographic digital elevation model (DEM) generation the stereographic generation of digital elevation models
45 (DEM; Shean et al., 2020; Dai et al., 2020a; Dille et al., 2021). Interferometric synthetic aperture radar (InSAR) can provide mm to cm-resolution line of sight displacements (e.g. Handwerger et al., 2019; Jacquemart and Tiampo, 2021; Manconi et al., 2018). Growing archives of high-resolution, open access Earth observation data remain largely untapped for landslide monitoring. In this study we use the data-rich 7 February 2021 Chamoli rock-ice avalanche as a case study for the remote identification of landslide precursory signs. We first introduce landslide hazards in the Himalaya with specific focus on the Chamoli event,

50 and then offer a general overview of remote sensing of slope instabilities. Next, we explain the methods used in the current study, and present and discuss the results.

1.2 Landslide hazard and risk in the Himalaya

Landslides occur in high mountain areas all over the world. ~~Landslide~~, and the risk is greatest ~~where zones of~~ in areas where high topographic relief ~~intersect~~ intersects with high population densities or infrastructure – which is the case across much of the Himalayan region. Over 50 million people live directly within the Himalaya, with a further 700 million living within associated watersheds (Dimri et al., 2019). A combination of extreme topographic relief, regular tectonic activity, high seasonal rainfall intensities, ~~glacierization~~, and steep slopes make the Himalaya particularly susceptible to landslides (Kirschbaum et al., 2019).

~~Several~~ In recent decades, several factors have contributed to raising landslide risk across the region ~~in recent decades~~: first, climatic warming has driven rapid thinning and retreat of Himalayan glaciers – which are currently losing over 10 Gt of mass per year (e.g. Kääb et al., 2012; Brun et al., 2017; Shean et al., 2020; Jakob et al., 2021; Hugonnet et al., 2021). Glacier retreat may contribute to a range of factors conducive to landslides, including a reduction in slope buttressing and an increase in meltwater availability (Holm et al., 2004; Fischer et al., 2006; Huggel et al., 2012; Kos et al., 2016; Coe et al., 2018; Dai et al., 2020a; Glueer et al., 2020). In addition to glacier retreat, permafrost degradation has also been documented to reduce slope stability (Gruber and Haeberli, 2007; Allen et al., 2011; Fischer et al., 2012; Krautblatter et al., 2013; Haeberli et al., 2017; Magnin et al., 2019; Pörtner et al., 2019; Patton et al., 2019; Deline et al., 2021). Second, increasing populations, economic growth, and infrastructure development in high-mountain valleys have greatly expanded the potential consequences of landslides. This second point is apparent for the Chamoli disaster, in which the majority of deaths occurred at hydropower plants that were recently built or were under construction (Shugar et al., 2021). Other factors, including changes in precipitation ~~pattern~~ patterns (e.g. Li et al., 2018; Kirschbaum et al., 2020) and land use (Cummins, 2019) may also contribute to evolving landslide hazard potential and associated risk.

1.3 The 2021 Chamoli hazard cascade

During the morning of 7 February 2021, a 26.9 ~~95% confidence interval 26.5–27.3~~ Mm^3 wedge of rock and ice detached from the north face of Ronti peak, a 5500 m ~~peak~~ elevation summit in the Uttarakhand Himalaya (Fig 1.). This wedge then dropped around 1800 m to the Ronti Gad valley floor, where it continued down-valley towards the Rishiganga and Dhauliganga rivers and transformed into a debris flow (Shugar et al., 2021; Cook et al., 2021). The collapse block was composed of ~~approximately~~ approximately 80% bedrock and 20% glacier ice. Frictional heat generation calculations suggest that most or almost all of the glacier ice melted during the 3400 m drop from the ~~collapse source to the hydropower stations~~ source to Tapovan hydropower station (Shugar et al., 2021). This melting of the ice ~~facition~~, combined with major sediment deposition at the confluence of the Ronti Gad and Rishiganga, increased the initial rock-ice avalanche's water content and converted it into a ~~debris flow. The resulting debris flow caused further downstream damage, leaving~~ highly-mobile debris flow which left 204 people missing or killed and destroying two hydropower stations.

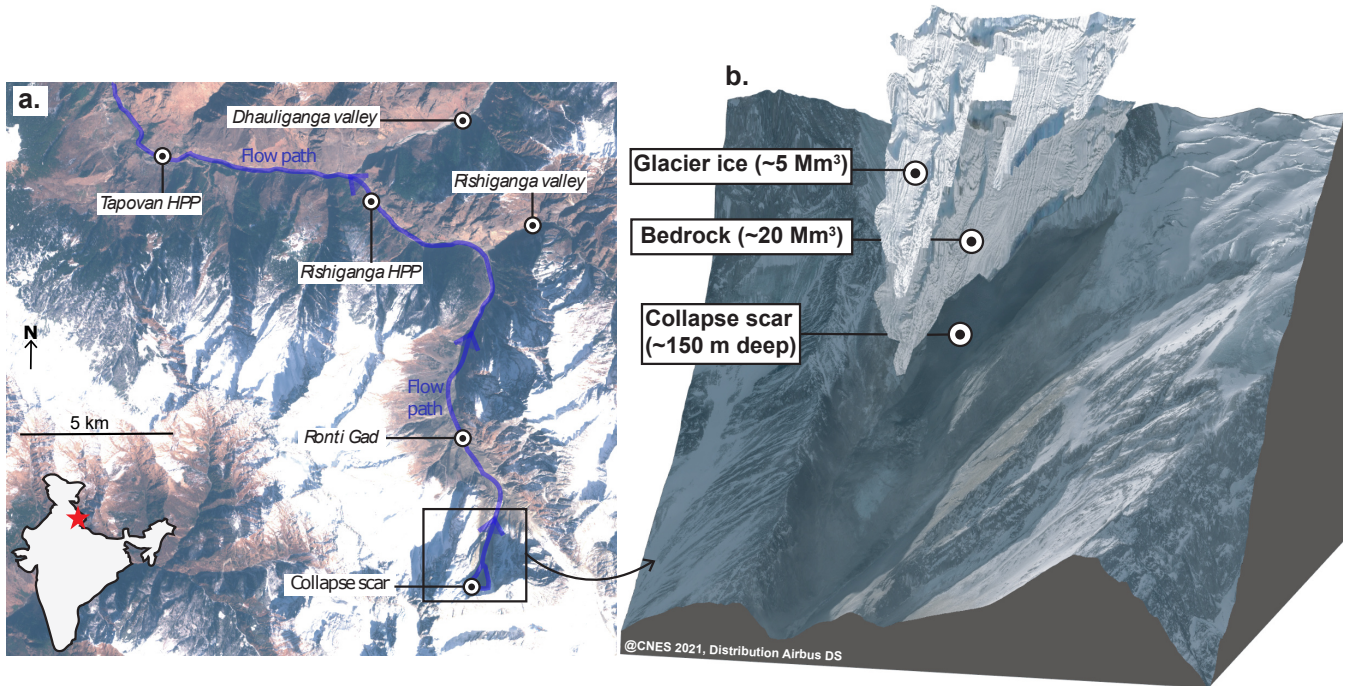


Figure 1. The 7th February Chamoli rock-ice avalanche: (a) shows the path of the collapse, along with key locations (HPP refers to hydropower plant) annotated on a 10th of February 2021 Sentinel-2 image (b) 3D visualization shows the post-collapse scar with reconstruction of the overlying bedrock and glacier ice.

1.4 Remote-sensing techniques

1.4.1 Feature tracking

85 Optical feature tracking is a versatile technique, which can be used to track surface motion by evaluating the relative position of features or patterns in repeat [satellite images or aerial photos imagery](#). Feature tracking has been applied to a variety of problems, including tracking post-seismic ground deformation (e.g. Leprince et al., 2007), [measuring-quantifying](#) glacier flow velocities (e.g. Bindschadler and Scambos, 1991; Heid and Käab, 2012; Millan et al., 2019; Van Wyk de Vries and Wickert, 2021), [and](#) [or](#) measuring landslide displacements (e.g. [Behling et al., 2014](#); [Lueicer et al., 2014](#); [Manconi et al., 2018](#); [Dai et al., 2020a](#); [Dille et al.](#)

90 =

1.4.2 Stereo-DEM generation

[Stereo-DEM generation uses two or more overlapping optical images to reconstruct surface topography. These images are acquired at the same time but from different viewing angles. Software implementing photogrammetric principles can then be used to derive elevation products \(such as DEMs\) from these images. With the recent availability of very high resolution satellite](#)

95 stereo imagery, these approaches can now be used to generate detailed DEM products over large spatial areas (e.g. Korona et al., 2009; Morin et al., 2016; Shean et al., 2016; Porter et al., 2018). Repeat DEMs obtained at different time periods can provide precise estimates of surface elevation change associated with many processes, including glacier change (e.g. Brun et al., 2017; Willis et al., 2018; Zheng et al., 2019; Shean et al., 2020), snow accumulation/melt (e.g. Deschamps-Berger et al., 2020; McGrath et al., 2019; Bhushan et al., 2021), volcanic deformation (e.g. Bisson et al., 2019) and landslide or debris flow events (e.g. van Westen and Lulie Getahun, 2003) (e.g. Behling et al., 2014; Aryal et al., 2012; Lucieer et al., 2007). The accuracy of feature tracking is limited by the spatial resolution of the imagery and the magnitude of displacements: in best case scenarios displacement maps may reach a precision of ~ 0.1 pixels (Leprince et al., 2007; Dille et al., 2021). For openly available Sentinel-2 imagery, this means that displacements of less than 1 m cannot be detected from a single image pair. Commercial imagery datasets are available with higher spatial resolution (e.g. 3 m for Planet Dove CubeSat, 0.3 m for WorldView) which may resolve smaller displacements (e.g. Stumpf et al., 2014), but are expensive to procure and process and do not offer systematic repeat coverage. Similarly, displacements may be mapped from high-resolution UAV imagery (Peppas et al., 2017), but this requires prior knowledge of the hazardous area and targeted acquisition campaigns.

1.4.2 InSAR

Satellite-based InSAR is a powerful tool for detecting small changes at the Earth's surface from space. It has been widely used to quantify ground displacements caused by processes such as earthquakes (e.g. Massonnet et al., 1993; Barba-Sevilla et al., 2018), groundwater extraction (e.g. Samsonov and d'Oreye, 2017; Motagh et al., 2017), volcanic unrest (e.g. Rosen et al., 1996; Tiampo et al., 2017), or landslides (e.g. Manconi et al., 2018; Handwerger et al., 2019; Dai et al., 2020b; Mondini et al., 2021; Jacquemart and Tiampo, 2021). By measuring the shift of the radar phase relative to earlier measurements of the same features, InSAR can provide measurements of ground deformation at millimeter and centimeter scales. Active radar sensors can image the Earth's surface through clouds and darkness, a major advantage over passive optical sensors (e.g. Massonnet and Feigl, 1998). Leveraging However, leveraging InSAR data for the detection and assessment of mass movements, however, is not without challenges is challenging. The oblique viewing geometry of radar satellites means that radar data can be rendered useless in areas of steep topography due to the effects of shadowing, foreshortening, and layover (Massonnet and Feigl, 1998; Wasowski and Bovenga, 2014). Finally, in In case of rapid displacements that surpass the phase-aliasing thresholds or dramatic changes in the surface cover or geometry, a loss of interferometric coherence can prohibit the quantification of (the full) ground deformation (Manconi, 2021). Despite these drawbacks, many studies have shown that InSAR can be successfully applied to assess stability of slopes even in high relief terrain (e.g. Manconi et al., 2018; Handwerger et al., 2019; Bekaert et al., 2020; Jacquemart and Tiampo, 2021).

1.4.3 Stereo-DEM generation

125 Stereo-DEM generation uses two or more overlapping optical images that were acquired at the same time from different viewing angles to reconstruct surface topography. Photogrammetric principles can then be used to derive DEMs from these images. With the increased availability of very high resolution satellite stereo imagery, these approaches can now be used to generate detailed DEM products over large spatial areas (e.g. Korona et al., 2009; Morin et al., 2016; Shean et al., 2016; Porter et al., 2018;

130 . Repeat DEMs obtained at different time periods can provide precise estimates of surface elevation change associated with many processes, including glacier change (e.g. Brun et al., 2017; Willis et al., 2018; Zheng et al., 2019; Shean et al., 2020), snow accumulation/melt (e.g. Deschamps-Berger et al., 2020; McGrath et al., 2019; Bhushan et al., 2021), volcanic deformation (e.g. Bisson et al., 2021), and landslide or debris flow events (e.g. van Westen and Lulie Getahun, 2003). In particular for landslide research, previous studies have used DEM differencing techniques to identify geomorphic changes (e.g. Corsa et al., 2022) and precursory motion (e.g. Higman et al., 2018; Dai et al., 2020a) on timescales ranging from years (e.g. Shugar et al., 2021; Geertsema et al., 2022) to decades (e.g. Higman et al., 2018; Lacroix et al., 2020).

135 1.5 Objectives

The objective of this study is to ~~evaluate the use of~~ the 7 February 2021 Chamoli rock-ice avalanche as a detailed case study to assess the potential and limitations of satellite-based landslide monitoring. We first assess the pre-collapse conditions of the 7 February 2021 Chamoli rock-ice avalanche, ~~in particular and then interpret them in a broader context. Our research question is:~~
140 ~~What was the scale and geometry of~~ Can the pre-collapse surface change, and what insight do these changes provide into ~~the collapse mechanisms? Would these pre-collapse datasets and tools be adequate to identify this hazardous slope without the prior knowledge of its failure?~~ remotely-sensed datasets be used automatically to identify the location or timing of the 7 February 2021 Chamoli rock-ice avalanche, and is it possible for these monitoring techniques to be upscaled for hazard monitoring on a regional or global scale?

2 Methods

145 We used a range of datasets and processing workflows to investigate the pre-collapse conditions of the Chamoli rock-ice avalanche:

1. Optical satellite imagery (Landsat and Sentinel-2) was used to investigate visible changes in the collapse region over the years to decades prior to the rock-ice avalanche
2. Feature tracking of optical satellite imagery (Sentinel-2, Planet, Cartosat-1, and SPOT7) was used to derive horizontal displacements
- 150 3. Sentinel-1 C-band radar imagery was used to calculate interferometric synthetic aperture radar (InSAR) displacement maps
4. Digital elevation models (DEMs) from optical satellite stereo-imagery (WorldView-1/2/3, GeoEye-1, Pleiades-HR, SPOT-7 and Cartosat-1) were used to derive vertical changes
- 155 5. ~~Sentinel-1 C-band radar imagery was used to calculate interferometric synthetic aperture radar (InSAR) displacement maps~~

2.1 Qualitative observations of slope change

We investigated three decades of pre-collapse optical satellite imagery to gain a preliminary understanding of pre-landslide changes. We documented changes in the north-facing slope of Ronti peak, which sourced the February 2021 rock-ice avalanche, using all available data from Landsat 5 (TM), Landsat 7 (ETM+), Landsat 8 (OLI), and Sentinel-2 with a cloud cover of less than 60%. We focused our observations on surface changes, including deformation and fracturing, and rock or ice avalanches originating from the collapsed block or surrounding area.

Our ability to detect change is limited by the spatial resolution of the imagery used (15-30 m for Landsat and 10 m for Sentinel-2). We examined a 31-year (1990-2021) time series of satellite imagery (Fig 2), including 122 Landsat 5 images, 43 Landsat 7 images, 34 Landsat 8 images, and 155 Sentinel-2 images. A full list of images is provided in the supplementary material, along with a brief description of any anomalous features.

2.1.1 Optical feature tracking

We used feature tracking with a range of medium (10 m) to high (2.5 m) resolution satellite imagery to evaluate the pre-collapse motion of the Ronti peak north slope. We used two different feature-tracking toolboxes: GIV [for rapid processing of Sentinel-2 data](#) (Van Wyk de Vries and Wickert, 2021) and AutoRIFT (Lei et al., 2021) [for processing Planet data as part of a pipeline also including orthorectification of imagery](#). Both GIV and AutoRIFT are based on three core components: a pre-processing module which applies one or more filters ([described below](#)) to images to enhance distinct surface features for tracking, a multipass 2D image correlator, and a post-processing module to identify and filter erroneous displacement values (Van Wyk de Vries and Wickert, 2021; Lei et al., 2021). The GIV toolbox ~~is written in MATLAB and~~ performs image cross correlation in the frequency domain, while AutoRIFT is ~~written in python/C++ and~~ performs the cross correlation in the spatial domain. Using GIV, we pre-processed the imagery using an orientation filter and ran the cross-correlation with a reducing window size from 20 to 5 pixels and a window overlap of 50%. In AutoRIFT we pre-processed the imagery with a Laplacian filter and used adaptive window sizes between 32 and 64 pixels with a skip rate of 8 pixels for the cross-correlation.

We calculated velocities using all available Sentinel-2 images through February 2021, excluding any images with a local cloud cover greater than 60% (based on the L1-C QA band cloud mask). A total of 155 images were available, for a total of 5237 image pairs with a time separation between 50 and 500 days. We processed these image pairs using GIV. We also resampled the velocity timeseries to monthly resolution (see Fig 4 c-g) using a weighted averaging scheme described in Van Wyk de Vries and Wickert (2021), [with weights based on the proportion of the time period within a given month](#).

We [also](#) downloaded all PlanetScope Dove Classic (4-band) Level-1B imagery with less than 20% cloud cover acquired between January 2020 and January 2021. We processed 4701 image pairs using AutoRIFT with [a](#) time separation of 100 to 350 days. The Near-infrared (NIR) band from the L1B images was orthorectified on the 2015 pre-event reference DEM (Bhushan and Shean, 2021) and the systematic median offset (computed over static, non-glacierized surfaces) was removed from each pairwise surface displacement map in both E-W and N-S directions. Despite the higher product resolution (3 m vs 10 m Sentinel-2 images) and use of a high-resolution DEM for improved orthorectification, the Planet velocity maps had a

190 high random background noise. We attribute this to spurious correlation over surfaces with varying shadow cover due to steep slopes and changing illumination, as the images were captured by different satellites during different times of the day/year. To compensate for this higher background noise, we chose a higher minimum temporal separation (100 days, compared to 50 days for Sentinel-2) between Planet image pairs when calculating time-averaged velocity maps. We also calculated displacements (using both GIV and AutoRIFT) on one pair of high-resolution Cartosat-1 images (Oct 2017 to Nov 2018).

195 We used this velocity data to evaluate whether the collapsed block moved prior to collapse – with a null hypothesis that the block moved no more than the surrounding ‘stable’ (non-glacierized) bedrock. ~~A~~ We tracked the motion of a medial bedrock ridge near the center of the collapsed block provides to measure the motion of the underlying rock, rather than simply bedrock, which is independent from the flow of the overlying glaciers. We divided the collapse block into three different regions alongside a zone of stable ground, and create a time series of average displacement for each zone.

200 **2.2 InSAR maps**

We processed Sentinel-1 data from the ascending and descending orbit tracks 56 and 63, respectively, to investigate whether the precursory motion of the collapse block could have been detected in radar interferograms. All radar data was downloaded from the Alaska Satellite Facility Distributed Active Archive Center (ASF DAAC). Because the descending track is heavily affected by layover artefacts, we only performed the full processing with data from the ascending orbit. We processed the data with the InSAR Scientific Computing Environment (ISCE; Rosen et al., 2012), removed the topographic phase using the 2015 pre-event WorldView DEM (Bhushan and Shean, 2021) composite (resampled to 8m), and masked out all pixels with an interferometric coherence of less than 0.3. Single look complex (SLC) images were multi-looked to 1 and 3 looks in azimuth and range, respectively. We generated 108 interferograms covering the period of January 2017 to November 2020, each spanning 12 days. We manually selected the best interferograms and performed unwrapping with the Statistical-Cost, Network-Flow Algorithm for Phase Unwrapping (SNAPHU; Chen and Zebker, 2002).

210

2.3 DEM generation

We produced multiple pre-event and post-event DEM products from very high-resolution (Maxar/DigitalGlobe WorldView-1/2/3, GeoEye-1 and Airbus/CNES Pleiades, 0.3 to 0.5 m GSD) and high-resolution (Airbus SPOT-7 and ISRO CartoSat-1, 1.5 m to 2.5 m GSD) satellite imagery captured between 2015 and February 2021. The DEM products were used to calculate the vertical motion of the collapse block from 2015 to February 10, 2021.

215 We used the NASA Ames Stereo Pipeline (Shean et al., 2016; Beyer et al., 2018) to process all of the images. For this particular study, we primarily used four products spanning two time periods: the 2015 pre-event WorldView DEM composite (Bhushan and Shean, 2021); an intermediate period, a 2018 pre-event DEM composite produced by averaging the November 2018 CartoSat-1 (Appendix A1) and December 2018 SPOT-7 (Appendix A2); and the February 10-11, 2021 post-event composite DEM derived from Pleiades and WorldView/GeoEye stereo imagery (Shean et al., 2021). We calculated the difference between three composite DEM products to create 2015-2018, 2015-2021, and 2018-2021 DEM of difference (DoD). The first 2015-2018 DoD provides insight into vertical changes in the hillslope prior to failure, while the ~~second~~ 2015-2021 DoD pro-

220

vides the volume and geometry of the collapsed block. We calculated an empirical uncertainty estimate for each DoD using the tiling method (Berthier et al., 2016; Miles et al., 2018; Jacquemart et al., 2020).

225 2.4 InSAR maps

~~We analyzed Sentinel-1 data from the ascending and descending orbit tracks 56 and 63, respectively, to investigate whether the precursory motion of the collapse block could have been detected from radar interferometry. All radar data was downloaded from the Alaska Satellite Facility Distributed Active Archive Center (ASF DAAC). Because the descending track is heavily affected by layover artefacts, we only performed the full processing with data from the ascending orbit. We processed the data with the InSAR Scientific Computing Environment (ISCE; Rosen et al., 2012), removed the topographic phase using the 2015 pre-event WorldView DEM (Bhushan and Shean, 2021) composite (resampled to 8m), and masked out all pixels with an interferometric coherence of less than 0.3. Single look complex (SLC) images were multi-looked to 1 and 3 looks in azimuth and range, respectively. We generated 108 interferograms covering the period of January 2017 to November 2020, each spanning 12 days. We manually selected the best interferograms and performed unwrapping with the Statistical-Cost, Network-Flow Algorithm for Phase Unwrapping (SNAPHU; Chen and Zebker, 2002).~~

3 Results

~~Where observation was possible, the different methods are in agreement: the slope fractured and was displaced on the order of tens of metres prior to the eventual collapse. The 2021 rock-ice avalanche was also preceded by several other large avalanches —although these were primarily sourced from an adjacent hanging glacier.~~

240 3.1 Qualitative observations of slope change

We identified four main types of processes in our 31 year optical satellite image time series:

1. Major ice avalanches (01-04/2000 and 09-10/2016): Large-volume ice avalanches, which originated from the steep hanging glacier to the west of the collapse block. These temporarily filled Ronti Gad with ice, snow, ~~debris~~ and sediment.
- 245 2. Minor snow or ice avalanches (2005, 2006, 2007, 2008, 2012, and 2015): Smaller volume avalanches, which may either have originated from the adjacent hanging glacier or the seasonal snowpack. These did not appear to infill the underlying valley with any significant quantity of material (with the exception of one ~500 m long snow/ice deposit in May 2006).
3. Minor landslides avalanches (2007, 2009, 2011, 2012, 2013, and 2015): Minor rockfalls or rock avalanches originating from Ronti peak, or the ~~weak~~ unconsolidated sediment on the flanks of Ronti Gad. These also do not appear to have deposited major volumes of sediment.
- 250 4. Opening and widening of cracks at the headwall of the collapse block (2016-2021): Gradual opening of a wide crack in the north face of Ronti peak.

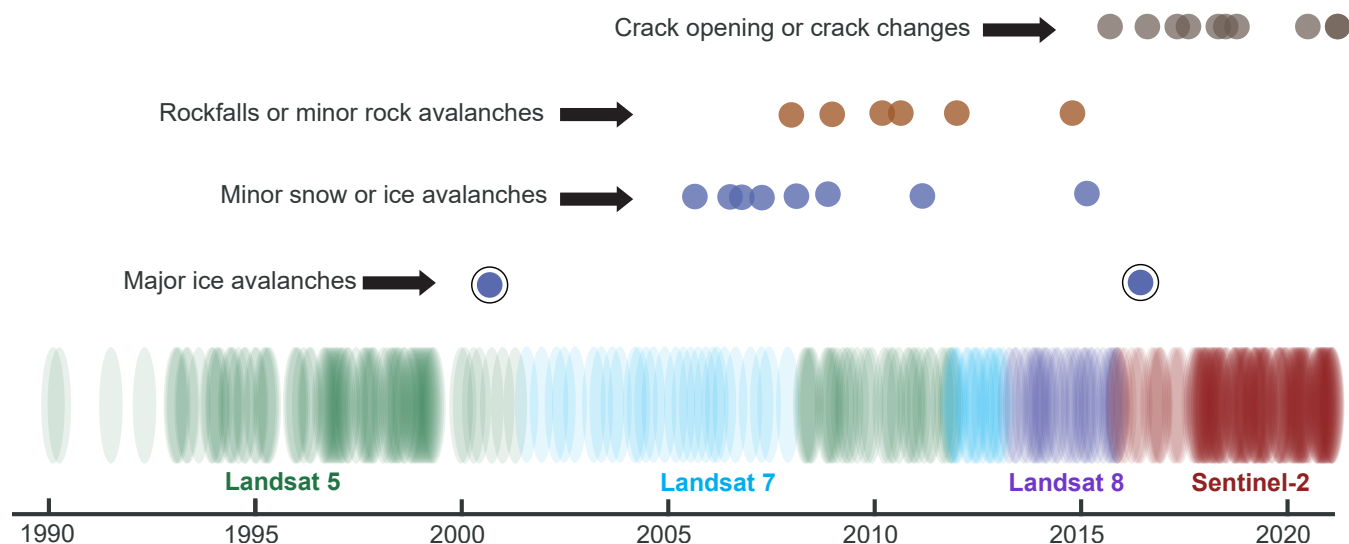


Figure 2. Timeline of images analysed for change at the Chamoli site prior to the 7th of February 2021 collapse, with major events or changes seen over this period. The first image (06/02/1990) was taken 31 years before the collapse, and the last image (05/02/2021) two days before the collapse.

We only interpret the 4th process type (crack opening) is a real sign of pre-collapse conditions. Minor rockfalls and snow/ice avalanches are a common feature of high relief, high slope active landscapes (e.g., Petley, 2012; Huggel et al., 2012; Vincent et al., 2015; K. . The major ice avalanches represent a serious geohazard in the upper Ronti Gad, but appear to relate to internal dynamics of the western hanging glacier rather than instability in the underlying bedrock. The area of these 2000 and 2016 major ice avalanches was estimated at 0.16 km² and 0.2 km², with melting and/or redistribution of the the resulting valley floor deposits within three years of the event (Shugar et al. (2021); Supplementary section 3.1). Regular large ice avalanches have been observed at many other hanging glaciers in active, high-mountain environments (e.g. Faillettaz et al., 2008; Vincent et al., 2015).

The conspicuous crack at the headwall of the failed block was first visible in optical imagery in March 2016, although its location roughly aligns with a pre-existing glacier crevasse – suggesting that minor crack opening in the bedrock may have preceded this date. The crack grew to approximately its maximum size by the end of 2018, and appeared to ~~reduce in depth or become infilled~~ become infilled with snow over the course of 2019 and 2020-2020 based on the amount of exposed bedrock on the rock walls. The crack widened further between 2018 and the 7 February 2021 collapse to a total width of 50-70 m, but less rapidly than the opening in 2016-2018. We confirmed ~~these observations~~ our observations of the crack opening with several very-high (~0.5 m) resolution images (Fig 3).

3.2 Optical feature tracking

Feature tracking provides the most complete spatio-temporal assessment of displacement of the methods used in this study – with data coverage from late 2015 until early 2021. We used results from the Cartosat-1 image pair and the Planet archive for

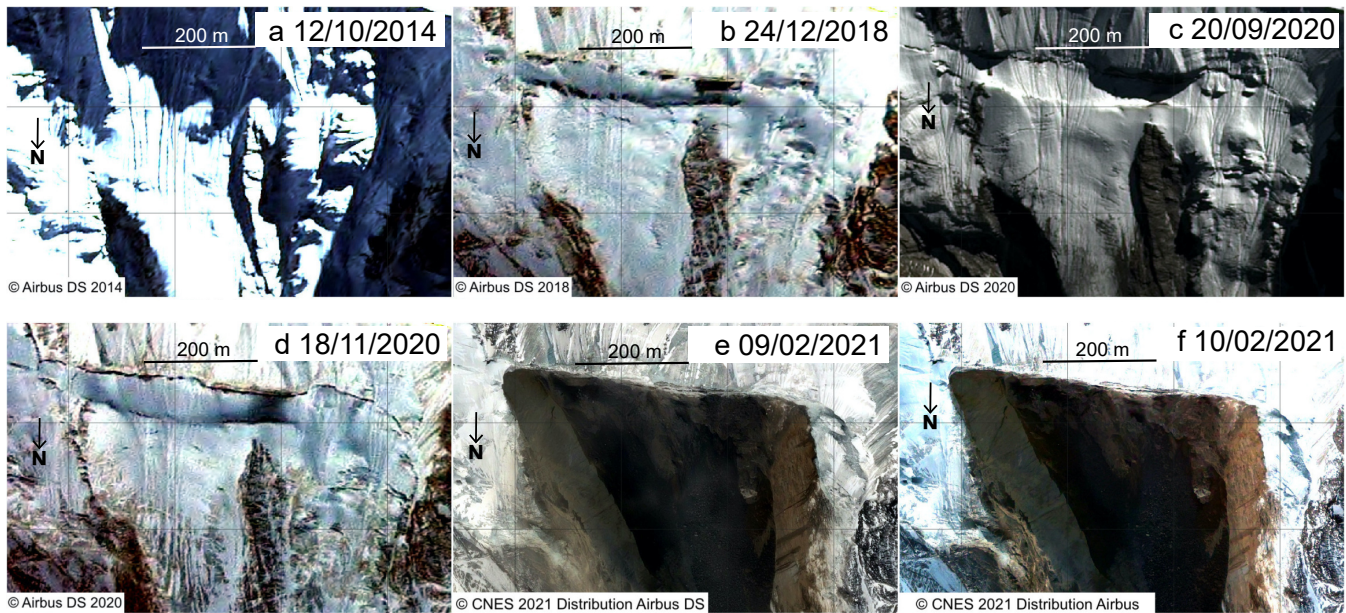


Figure 3. Time series of headwall crack opening in high-resolution optical images from SPOT-7 and Pleiades-HR.

validation of the Sentinel-2 displacements. In all three cases, the collapsed block (most notably, the bedrock ridge at the centre
270 of this block) exhibited displacements exceeding the background noise level on stable bedrock ($<1 \text{ m yr}^{-1}$).

The horizontal velocity of the collapsed block ranged from around 5 m yr^{-1} to 20 m yr^{-1} , with the most rapid motion
occurring in the summers of 2017 and 2018 (see Fig 4 d-g). We do not observe an increase in velocity of the collapsed block
immediately prior to its failure in February 2021. The Sentinel-2 image record includes 7 cloud-free images from early 2021,
including one image taken two days prior to the collapse, therefore this lack of speed-up is unlikely the result of a temporal data
275 gap. Periods with the highest block velocity (2017-2018) correspond to periods of greatest increase in headwall crack width –
particularly the summers of 2017 and 2018. This is consistent with motion occurring on the entire collapsed block, rather than
only on the glaciers or a superficial layer of rock.

Total 2016-2021 horizontal displacements were $\sim 20\text{-}30 \text{ m}$ (Fig 4a), ~~of similar~~ which is similar in magnitude to the width
of the crack as measured directly from Sentinel-2 imagery. ~~Projecting these horizontal displacements onto the steep surface~~
280 ~~slope (mean~~ Due to the steep topography (mean slope of 42.6°) results in an apparent increase of $\sim 36\%$, or $\sim 25\text{-}40$, the
visible horizontal motion does not account for all of the true deformation. After correcting for the viewing angle, the total block
motion is 25 - 40 m. Overall, the feature tracking results demonstrate that the collapse block was mobile several years prior to
its collapse in 2021.

3.3 DEM analysis

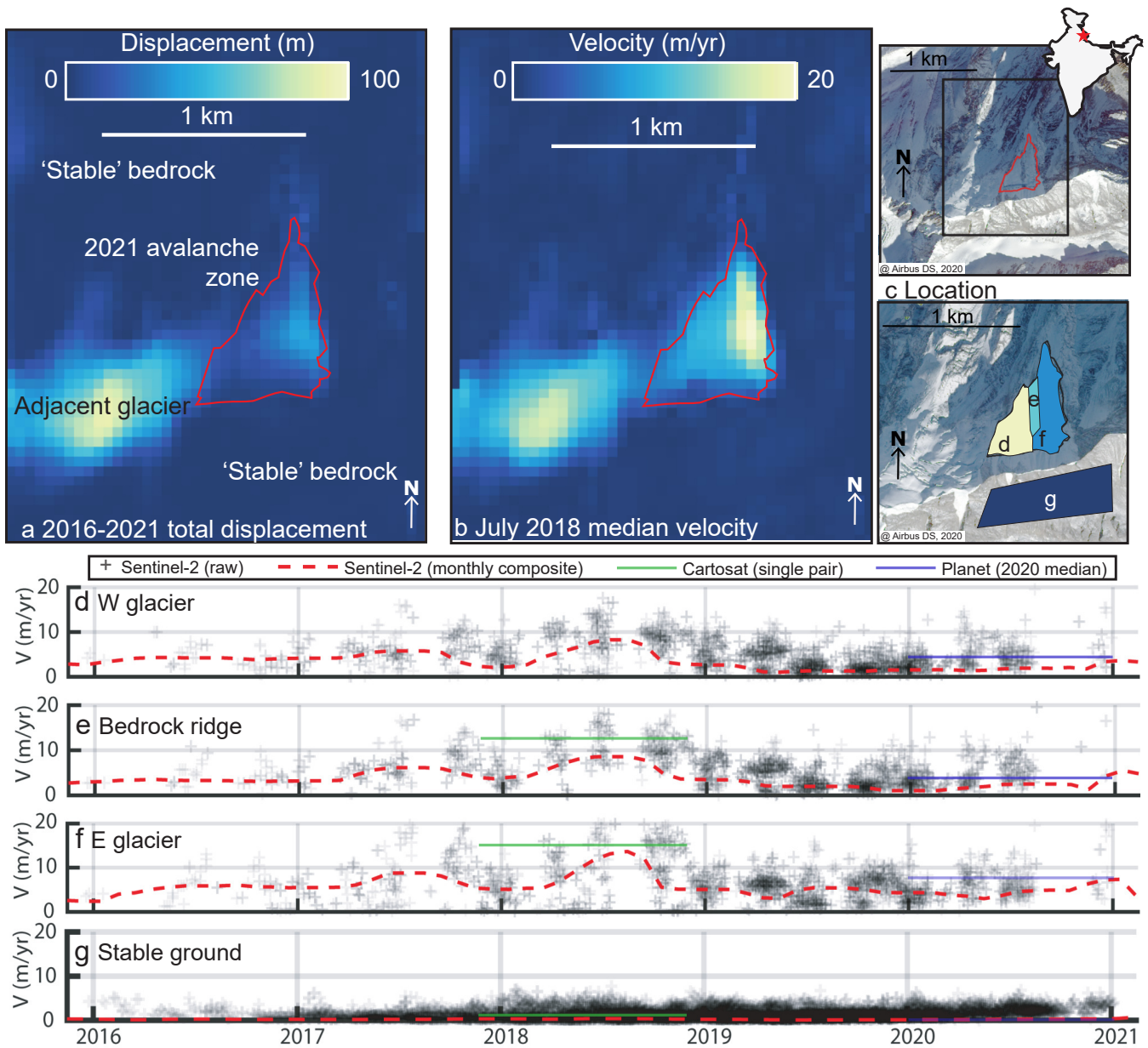


Figure 4. Surface displacement and horizontal velocity from optical image feature tracking. (a) shows the total displacement over the entire Sentinel-2 era, (b) shows a snapshot velocity during an episode of rapid displacement in Summer 2018, and (d)-(g) show time series of velocity averaged across specific zones shown in (c). Note the episodes of rapid displacement in 2017-18 relative to 2016 or 2020, corroborated by the Cartosat-1 and Planet derived velocities.

285 We calculated the geometry of the collapsed block, equal to the zone of negative elevation change in the 2018-2021 DoD (Fig 6e; volume = 26.9 95% confidence interval 26.5-27.3 Mm³; Shugar et al. (2021)). The earlier DoD (2015-2018) shows a very

different pattern (Fig 6b), with a 100 m wide zone of elevation loss at the upper altitude limit of the collapsed block ('headwall crack') and a broad zone of elevation gain over the remainder of the block ('bulge'). The magnitude of this pre-collapse elevation loss is greatest in the central and western portion of the headwall crack, while the elevation gain is most pronounced on the central and eastern portions of the bulge. The DoD uncertainties scale inversely with the size of area (number of pixels) considered: ± 4.2 m, 1.7 m, 7.3 m, and 2.7 m (10 by 10 m); ± 3.0 m, 0.8 m, 4.7 m, and 1.8 m (50 by 50 m); ± 2.4 m, 0.2 m, 3.8 m, and 1.1 m (250 by 250 m) for the 2015–2018 Cartosat, 2015–2018 SPOT, 2018–2021 (SPOT) and 2015–2021 DoDs respectively.

DEM analysis further confirms the results from direct image observations and feature tracking—large changes occurred on the collapsed block prior to its collapse. The zone of negative elevation change is wider than the crack as directly observed in optical imagery, which may result from limits in the DEM resolution or partial collapse of the surrounding rock or ice into the crack.

Elevation change of the avalanche zone pre- and post-collapse. (a) SPOT-7 true color composite image from September 2020 with location of cross-sections A and B for context, (b) and (c) provide DoD maps of different time periods, while (d) and (e) show two cross-section profiles (a) across the DoD. Cross-sectional uncertainties are assigned for an area equal to the length of the section line multiplied by the pixel size.

3.3 InSAR maps

Even with knowledge of the location of the failed block, the processed interferograms do not allow for a pre-collapse identification of the instability on Ronti Peak. Of the 108 available interferograms, roughly half exhibited a complete loss of coherence, largely due to snow cover (November through May). Good quality interferograms are limited to summer months, and on the collapse block, coherence is only retained on the ice free part at the bottom of the wedge. The upper, glacier-covered part of the collapse block remains decorrelated, likely due to shadowing and glacier/snow cover. Figure 5a highlights the very low radar backscatter in this zone, and Figure 5b/c confirms the spatial agreement between the loss of coherence and glacier cover. Data gaps lower in the valley are also related to loss of coherence, possibly due to vegetation cover or moisture variability. Many interferograms are characterized by high amounts of noise, likely from variable atmospheric properties or other artefacts.

A high quality interferogram from July 2020 (Fig. 5b) does not indicate any motion on the lower part of the collapse block in the summer prior to the failure, but ~~this cannot be assessed~~ it is impossible to determine whether this is consistent in other interferograms of that year due to high noise levels. Areas of high coherence are small and discontinuous on the collapse block, making it hard to determine any changes. In less steep terrain north-west of the collapse block, the motion of a rock glacier (on the order of cm yr^{-1}) can ~~consistently be detected in the interferograms~~ be detected consistently in all interferograms that remain coherent over that part of the image (Fig 5b). This highlights that the reliability and information content of InSAR velocity maps can be highly variable even across a small study area. Despite its sensitivity, InSAR is not able to provide any conclusive information about the pre-failure conditions of the collapse block in this challenging terrain.

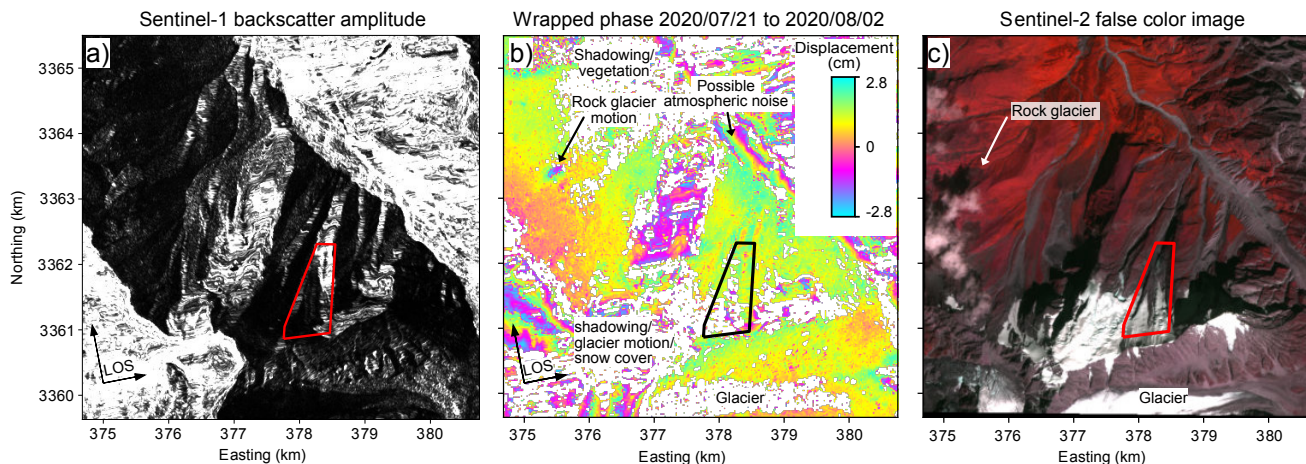


Figure 5. Sentinel-1 radar backscatter amplitude from the ascending orbit [track 56](#) (a), wrapped phase (0 to 2π or ± 2.8 cm) ~~ascending-orbit~~ interferogram from July 2020 (b) and corresponding false color image (c). Large areas of low coherence (masked as white) and patchy coverage illustrate the complexities of InSAR monitoring in high alpine terrain. The avalanche block is outlined in black and red.

3.4 DEM analysis

320 We calculated the geometry of the collapsed block, equal to the zone of negative elevation change in the 2018-2021 DoD (Fig 6c; volume = 26.9 [95% confidence interval 26.5-27.3] Mm³ ; Shugar et al. (2021)). The earlier DoD (2015-2018) shows a very different pattern (Fig 6b), with a ~100 m wide zone of elevation loss at the upper altitude limit of the collapsed block ('headwall crack') and a broad zone of elevation gain over the remainder of the block ('bulge'). The magnitude of this pre-collapse elevation loss is greatest in the central and western portion of the headwall crack, while the elevation gain is most
 325 pronounced on the central and eastern portions of the bulge.

DEM analysis further confirms the results from direct image observations and feature tracking – large changes occurred on the collapsed block prior to its collapse. The zone of negative elevation change is wider than the crack as directly observed in optical imagery, which may result from limits in the DEM resolution or partial collapse of the surrounding rock or ice into the crack.

330 4 Discussion

The pre-collapse motion of the avalanche block raises important questions about the causes and timing of the ~~slope failure~~
February 2021 Chamoli rock-ice avalanche. In this section, we ~~explore the answers to these questions~~ use this disaster as a case study to discuss the potential and limitations of satellite data for remote hazard monitoring. Furthermore, we explore the conditions of the collapse using our multi-dataset observations, evaluate whether the location or timing of the collapse could
 335 have been identified beforehand.

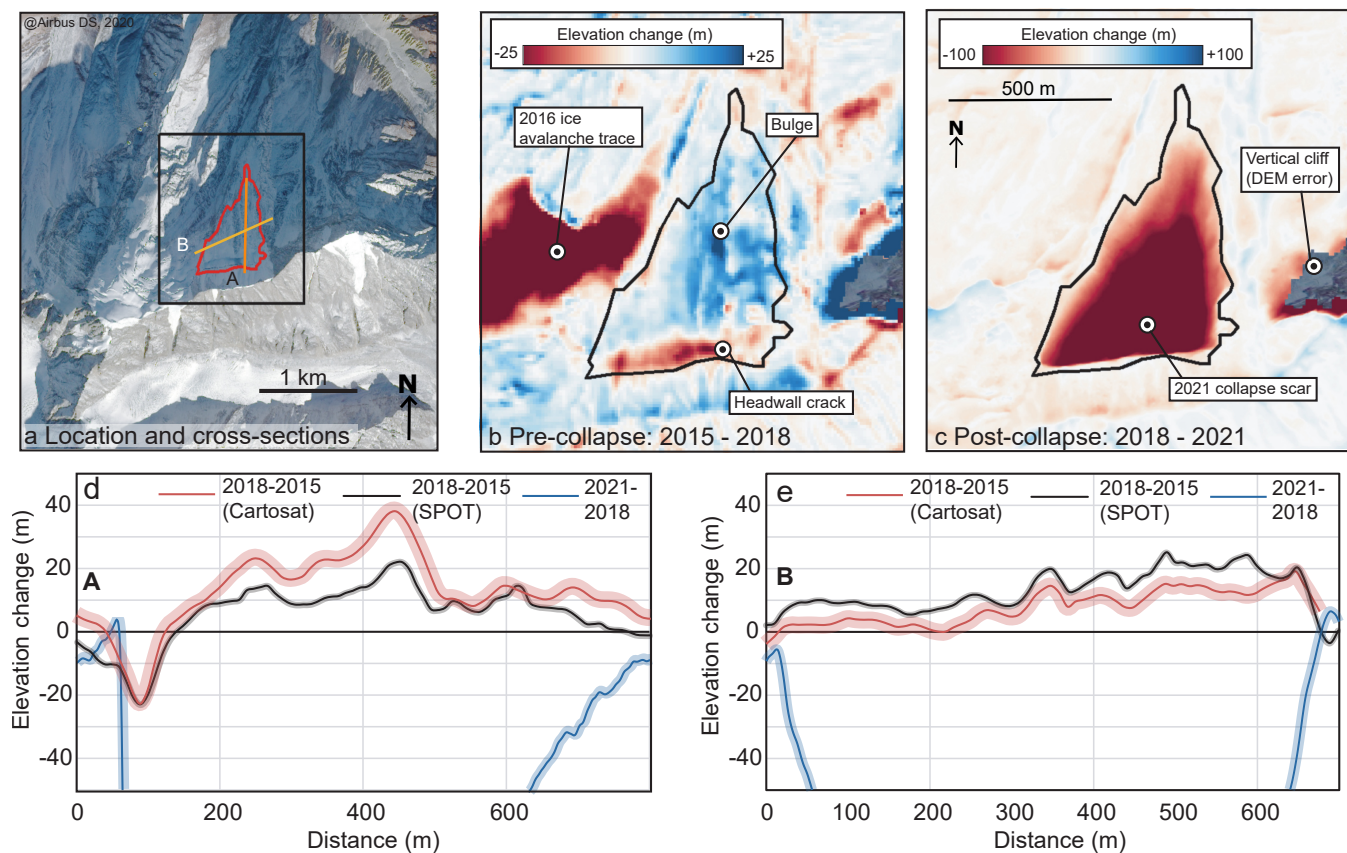


Figure 6. Elevation change of the avalanche zone pre- and post-collapse. (a) SPOT-7 true color composite image from September 2020 with location of cross-sections A and B for context, (b) and (c) provide DoD maps of different time periods, while (d) and (e) show two cross-section profiles (a) across the DoD. Cross-sectional uncertainties are assigned for an area equal to the length of the section line multiplied by the pixel size.

4.1 Future perspectives: remote-sensing based hazard monitoring

Our work on the Chamoli avalanche took place after the collapse, with the full knowledge of the position of the avalanche source. This work is useful for better understanding the conditions of the slope collapse. However, to be directly useful for hazard monitoring and prevention, these techniques must identify avalanche locations and sizes before – rather than after – they occur. The key questions therefore remain: would it have been possible to identify the Chamoli landslide prior to its collapse using the methods used in our study, and can these methods be applied elsewhere to identify future failures?

The qualitative analyses of optical satellite images, feature tracking results, and DEM analysis all indicate that precursory signs of slope failure were detectable. Satellite images show a crack growing over the 5 years prior to failure (Fig 3), feature tracking reveals tens of metres of horizontal displacement of the collapsed block, and DEM differences show tens of metres of vertical elevation change over the collapsed block. Combining this information with background knowledge about Chamoli

district, such as the extreme relief, steep slopes, and historic avalanches, it would in principle have been possible to identify this as an unstable slope with high collapse potential.

While the data are sufficient to identify precursory signs of this rock-ice avalanche after the collapse has already occurred, there are important limitations to their use for automated hazard monitoring and ~~then discuss the potential and limitations of satellite data for remote hazard monitoring~~—pre-collapse detection of unstable slopes. The first key limitation is the very low signal to noise ratio of feature tracking horizontal velocity maps, DEM-derived elevation change maps, and InSAR velocity maps in the steep terrain most susceptible to slope failure. For feature tracking, the noise level of the composite 2016-2021 mean velocity maps is low (<1 m per year). However, the background noise level (as evaluated over stable bedrock) of individual velocity maps is much higher – and in some cases comparable to the magnitude of the signal (~5-20 m per year). For the DEMs, artifacts range from metres to tens of metres in scale, and additional "noise" is introduced by real elevation changes from glacier and snowpack change (Fig 7b). While these issues with false positives can be mitigated, this is challenging without knowing the signal of interest.

InSAR, while also being susceptible to false positives, is additionally prone to false negatives. The north-facing aspect of Ronti peak provides a twofold challenge: the illumination of the slope is limited (low backscatter, Fig 5a), and any motion – assuming it is largely in the direction of the steepest slope – is oriented in the direction in which the radar instrument is least sensitive. Additionally, the non-glacierized area of the collapse wedge is small, making it challenging to identify fringe patterns amongst the noise. Furthermore, with the largest velocities reaching tens of meters per year, the InSAR measurements are prone to phase aliasing and underestimation of the true displacement. Sentinel-1 InSAR would not have provided an adequate tool for monitoring in this case, even with knowledge of the location of the instability.

The second key limitation is that none of the datasets produced in this work could predict the timing of collapse. While most methods pick up precursory signs of slope failure, these begin almost five years prior to eventual collapse. The largest measured changes did not occur immediately prior to failure, but rather preceded failure by around three years. Mao et al. (2022) propose that abrupt growth of the 'summit' crack (which they term bergschrund) and lateral cracks is visible in the 5 February 2021 Sentinel-2 image (2 days prior to collapse). This 'summit' crack was, however, already prominently visible and growing over the 5 years prior to collapse (e.g. Figure 2), and the proposed lateral cracks do not precisely correspond to the margins of the eventual collapse zone. In addition, the proposed crack growth episode visible was not associated with any detectable peak in displacement (Figure 4). Even with the knowledge that the collapse occurred on 7 February 2021, signs pointing to an imminent collapse in remote sensing data from late 2020 or early 2021 are highly ambiguous. Tiwari et al. (2022) show that seismic signals were detectable from the Chamoli bloc as early as 2.5 hours prior to collapse. While they do not explore how easily the pre-collapse signals would have been detectable without prior knowledge of the event, they do note that the ~ 15 minutes between initial collapse and impact of the Tapovan dam would have enabled evacuation if a local early warning system had been in place.

One final limitation is related to the immense size of hazardous areas relative to the scale of hazards themselves. The Chamoli collapsed block had an area of around 0.25 km², while the Himalaya cover over half a million km². Any methods aimed at automatically detecting hazards prior to their occurrence must have a low 'false positive' (identified as a hazard in the database,

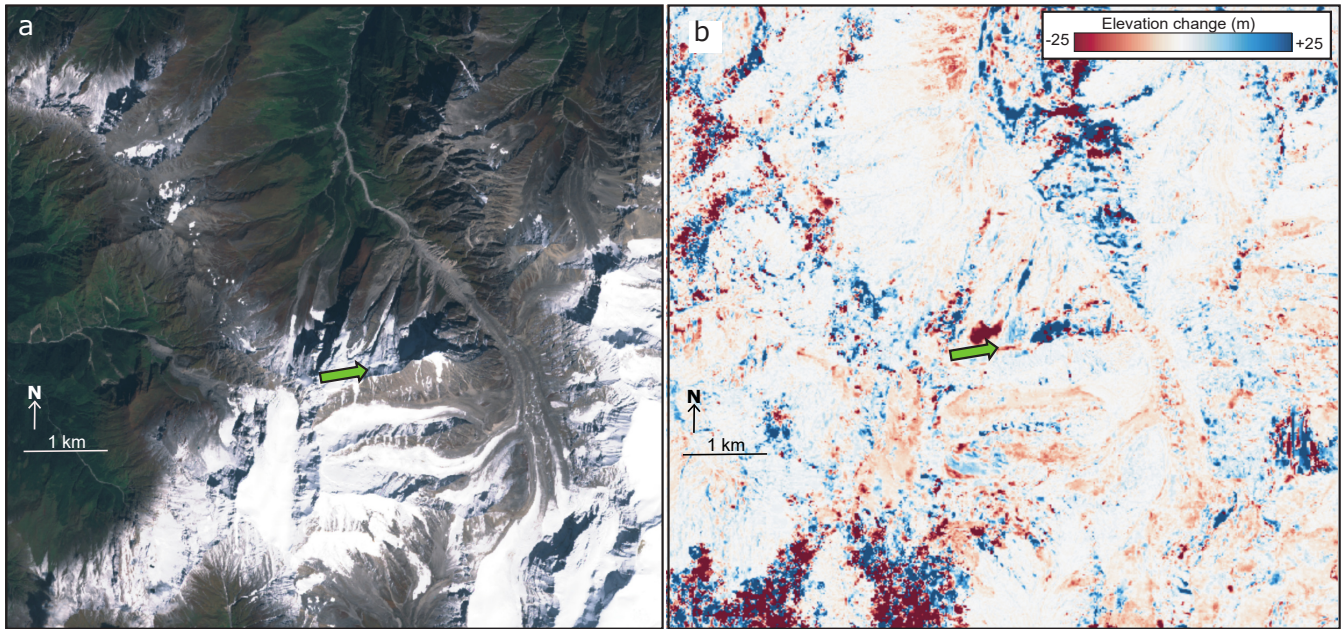


Figure 7. Optical satellite image (a: Sentinel-2; 28th of September 2020) and DoD (b; 2018-2015) of the Chamoli collapse site. Note the large number of steep slopes, complex terrain, and high noise levels in the DoD. In order to be useful for hazard prevention, these methods need to be able to identify potentially hazardous slopes without prior knowledge about collapses (e.g. green arrow shows the location of the headwall crack).

but not of real concern) rate, or any resulting database will be populated primarily with these incorrectly flagged regions. This becomes a major challenge when considering the high incidence of noise and artifacts in feature-tracking derived displacement or DoD maps (e.g. Figure 7). In addition, any hazard detection methods involving manual intervention, for instance an expert assessment of crack growth across a timeseries of optical satellite images, is not feasible on a large scale and will be limited to

385 previously identified zones of high hazard.

4.2 Three-dimensional block motion

We examined the three-dimensional motion of the collapse block as a first step towards understanding the Chamoli rock-ice avalanche collapse mechanism(s). Rotation and translation are the two primary modes of landslide motion (e.g. Záruba and Mencl, 2014), with each having a distinct surface displacement pattern. We used a combination of horizontal displacement

390 (feature tracking), vertical displacement (2015-2018 DoD), collapse block thickness (2018-2021 DoD), and post-landslide topography to calculate the dominant mode of pre-collapse motion for the Chamoli collapse block.

We compared our observations of vertical and horizontal slope displacement to a synthetic displacement, with the hypothesis that all of the observed change could be explained by translation. To model this translation, we set the direction of motion to

that of the steepest slope (\sim NNE) and its magnitude to 20 m. The displacement magnitude is chosen to match our observed
395 horizontal displacement from feature tracking - and is consistent with the findings of Qi et al. (2021).

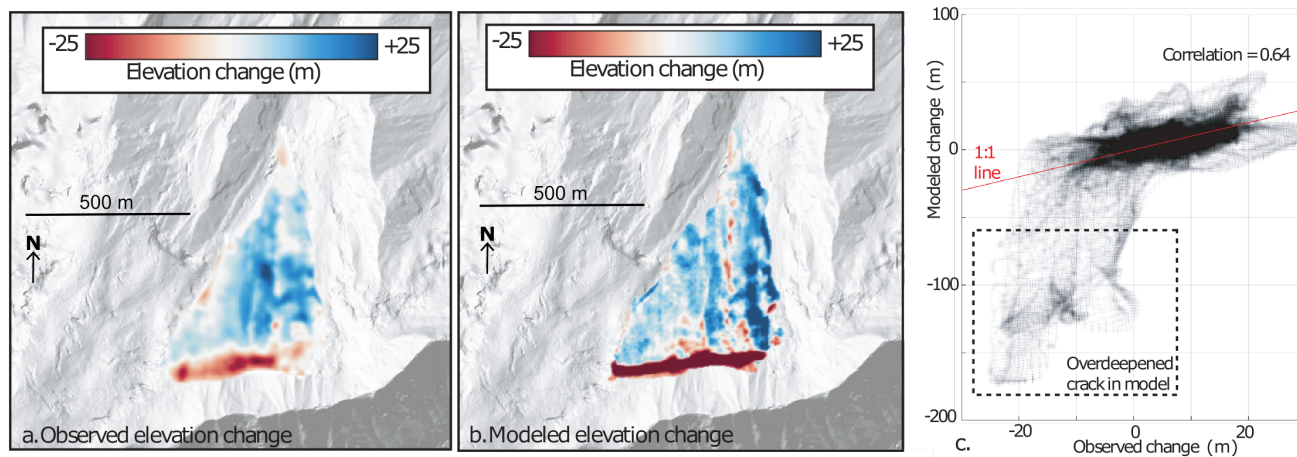


Figure 8. (a) Observed and (b) modeled elevation change of the Chamoli landslide block prior to collapse. The modeled scenario (b) is based on 20 m of pure downslope translation. (c) shows a scatterplot comparing each observed and modelled pixel.

Figure 8 shows a comparison between the observed change in surface elevation of the landslide block, and the modeled change. The pattern of elevation change is similar for the observed and modeled cases – both exhibit a deep summit crack, bulging in the lower collapse zone, and greater elevation gain on this bulge to the east relative to the west. The 2D correlation score is 0.64, with the greatest model-data difference at the headwall crack, which is as much as 150 m deeper in the model
400 case. These results are consistent with the Chamoli collapsed block moving downslope by translation in the years prior to collapse.

4.3 A possible avalanche triggering mechanism

A viable triggering mechanism for the Chamoli landslide must explain both the lag between the initial instability and collapse, and the timing of the collapse – in the middle of the winter. Syn-collapse seismic signals show that there was no seismic trigger
405 for the collapse (Pandey et al., 2021; Shugar et al., 2021; Cook et al., 2021). Nearby meteorological stations and reanalysis data reveal heavy snowfall and a ~ 5 K positive temperature anomaly in the week preceding collapse, as well as a temperature inversion in the valley (e.g. Pandey et al., 2021; Dandabathula et al., 2021; Zhou et al., 2021; Shugar et al., 2021). On the longer term, this region has warmed ~ 0.14 K per decade (Qi et al., 2021; Shrestha et al., 2021).

Zhou et al. (2021) and Dandabathula et al. (2021) propose that this sudden temperature increase may have triggered the
410 collapse, and Rana et al. (2021) associates it with lubrication of pre-existing fractures via melting of fresh snow. Kropáček

et al. (2021) and Pandey et al. (2021) suggest that loading from heavy snowfall may have contributed to the failure. Despite the positive temperature anomaly, temperatures at the collapse altitude (~ 5000 m) would have been below freezing point on the day of collapse, and liquid water would not have been present at the surface (Shugar et al., 2021; Dandabathula et al., 2021). Positive summer temperatures (Shrestha et al., 2021) and a steep surface slope of the collapse block will have prevented strong cumulative surface loading of the collapse block through snow deposition. Existing hypotheses do not provide strong mechanistic links between observed meteorological changes and the slope failure.

The stability of a slope can be described by the balance between two terms: driving forces (F_D) and resistive forces (F_R). Driving forces are primarily gravitational, while resistive forces are primarily related to slope cohesion and friction. For a detached wedge such as the Chamoli collapse block, dominant resistive forces are likely friction along the margins and base of the collapsed block. The balance between these two forces is known as the factor of safety FS :

$$FS = \frac{F_R}{F_D} \quad (1)$$

A slope is considered unstable when its factor of safety falls below 1 (e.g. Záruba and Mencl, 2014; Das and Sivakugan, 2016).

The Chamoli collapse area is composed of heavily jointed bedrock (e.g. Shugar et al., 2021). A pure translational pre-collapse motion is consistent with a collapse block basal shear plane along a single bedding plane. High-resolution post-collapse satellite imagery also suggests that the detachment occurred along a bedding plane. This failure plane may have been superficially weakened by freeze-thaw fracturing (Qi et al., 2021; Kropáček et al., 2021; Shrestha et al., 2021), or at greater depth by changes in permafrost conditions (e.g. Gruber and Haeberli, 2007; Krautblatter et al., 2013). The surface velocity peaks in summers 2017 and 2018 suggest that surface meltwater may have reached into the later failure surface. Meltwater infiltration may directly impact friction (F_D), and in a delayed way also alter ground temperatures through advection of heat and release of latent heat upon refreezing. Gruber and Haeberli (2007) note that advection-driven melt of permafrost thaw corridors may drive destabilization of large volumes of rock. Deep permafrost thaw may occur over long timescales (e.g. Gruber and Haeberli, 2007; Krautblatter et al., 2013), and provides one potential explanation for the 5-year lag between initial instability and collapse.

The deep headwall crack provides accommodation space for cumulative snow accumulation and loading, and also limits the melting of accumulated snow by reducing its surface exposure. Observations of elevation change over 2015-2018 show the opening of a crack at least 25 m deep at the collapse block headwall (Fig 8a), although DEMs may underestimate the true depth of the crack due to viewing angle, slope geometry, and stereo DEM processing parameters. The purely translation model of block motion (Fig 8b) suggests that the true crack depth would have been closer to 150 m. Snow, ice, or rock debris loading within a headwall crack would exert a horizontal force on the collapse block. This horizontal force ('push') acts to reduce the factor of safety both by directly increasing the driving force of the collapse block, and reducing the angle between the driving force vector and slope direction (equivalent to an increase in slope, see Appendix B).

Accumulation of snow or ice in the crack is visible in optical satellite imagery, with additional input from snow/ice avalanches from the overlying slope (e.g. Fig 3b-d). A storm in the days preceding the 7th February collapse brought substantial snowfall to the Chamoli region, with local snowfall estimates ranging from 8.5 to 48 mm water equivalent of precipitation (Shugar et al. (2021); estimates from local weather stations and Weather Research and Forecasting Model). We use these data to calculate the potential range of snow loading on the collapsed block, which is equivalent to a slope-parallel force of 7000-40,000 kN (Appendix A3). Considering the total precipitation between crack initiation (March 2016) and collapse (February 2021) this rises to 6.3×10^9 N to 9.9×10^9 N, or 2-3% of the total driving force of the collapse block.

In the absence of in-situ instrumentation and observations, it may not be possible to determine the exact cause of the failure at Chamoli. Nevertheless, we propose a mechanism which is compatible with both the lag between initial instability and collapse, and the timing of the eventual collapse. Snow and ice loading in the headwall crack would progressively increase the driving force of the collapse block, while meltwater infiltration and permafrost degradation in a bedrock fracture would steadily reduce its resistive forces (basal friction). The combination of these two processes would reduce the factor of safety and pre-condition the block for failure, with the early February positive temperature anomaly and loading from snowfall providing a final driver for mid-winter collapse.

4.4 Future perspectives : remote-sensing based hazard monitoring

~~Our work on the Chamoli avalanche took place after the collapse, with the full knowledge of the position of the avalanche source. This work is useful for better understanding the conditions of the slope collapse. However, to be directly useful for hazard monitoring and prevention, these techniques must identify avalanche locations and sizes before—rather than after—they occur. The key questions therefore remain: would it have been possible to identify the Chamoli landslide prior to its collapse using the methods used in our study, and can these methods be applied elsewhere to identify future failures?—~~

~~Several factors suggest that the available pre-collapse data may have been useful for identifying the Chamoli rock-ice instability. Careful qualitative analyses of optical satellite images, feature tracking, and DEM analysis show clear precursory signs of slope failure around the Chamoli collapsed block. Satellite images show a crack growing over the 5 years prior to failure (Fig 3), feature tracking reveals tens of metres of horizontal displacement of the collapsed block, and DEM differences show tens of metres of vertical elevation change over the collapsed block. Combining this information with background knowledge about this region, such as the extreme relief, steep slopes, and historic avalanches, it would in principle have been possible to identify this as an unstable slope with high collapse potential.—~~

~~While the data are sufficient to identify precursory signs of this rock-ice avalanche, there are important limitations to their use. The first key limitation is the very low signal to noise ratio of these data in the steep terrain most susceptible to slope failure. For feature tracking, the noise level of the composite 2016-2021 mean velocity maps is low (<1 m per year). However, the background noise level (as evaluated over stable bedrock) of individual velocity maps is much higher—and in some cases comparable to the magnitude of the signal (~5-20 m per year). For the DEMs, artifacts range from metres to tens of metres in scale, and additional "noise" is introduced by real elevation changes from glacier and snowpack change (Fig 7b). While these issues with false positives can be mitigated, this is challenging without knowing the signal of interest.—~~

InSAR, while also being susceptible to false positives, is additionally prone to false negatives. The north-facing aspect of Ronti peak provides a twofold challenge: the illumination of the slope is limited (low backscatter, Fig 5a), and any motion—
480 sensitive. Additionally, the non-glacierized area of the collapse wedge is small, making it challenging to identify fringe patterns amongst the noise. Furthermore, with the largest velocities reaching tens of meters per year, the InSAR measurements are prone to phase aliasing and underestimation of the true displacement. Sentinel-1 InSAR would not have provided an adequate tool for monitoring in this case, even with knowledge of the location of the instability.

Optical satellite image (a: Sentinel-2; 28th of September 2020) and DoD (b; 2018-2015) of the Chamoli collapse site. Note
485 the large number of steep slopes, complex terrain, and high noise levels in the DoD. In order to be useful for hazard prevention, these methods need to be able to identify potentially hazardous slopes without prior knowledge about collapses (e.g. green arrow shows the location of the headwall crack).

The second key limitation is that none of the datasets produced in this work could predict the timing of collapse. While most methods pick up precursory signs of slope failure, these begin almost five years prior to eventual collapse. In addition, the
490 largest magnitude changes did not occur immediately prior to failure, but rather preceded failure by around three years. Even with the knowledge that the collapse occurred on 7 February 2021, there are no obviously anomalous signs that a failure was imminent in late 2020 or early 2021.

One final limitation is related to the immense size of hazardous areas relative to the scale of hazards themselves. The Chamoli collapsed block had an area of around 0.25 km², while the Himalaya cover over half a million km². Any methods aimed at
495 automatically detecting hazards prior to their occurrence must have a low ‘false positive’ (identified as a hazard in the database, but not of real concern) rate, or any resulting database will be populated primarily with these incorrectly flagged regions. This becomes a major challenge when considering the high incidence of noise and artifacts in feature-tracking derived displacement or DoD maps (e.g. Figure 7).

Overall, forecasting the 7 February 2021 Chamoli rock-ice avalanche prior to its occurrence from remotely sensed datasets
500 would have been very challenging, and certainly not routine work using well-established methods. Current image ~~resolutions~~resolution, characteristics, and processing algorithms result in noise levels on a similar order to the signal itself. Only the joint interpretation of feature tracking results, DEM differences, and satellite images ~~reveal~~reveals clear precursory signs of slope instability. In addition, none of the data in this study are able to adequately forecast the timing of collapse. As such, current archives of satellite images do not currently appear to be practical for forecasting individual events. At the same time, this should not
505 prevent remote monitoring of hazardous zones, particularly when adjacent to vulnerable areas. Every slope failure will exhibit a different range of pre-collapse signals, and new instabilities might be recognized in some cases. Even though the forecasting of individual events remains a challenge, these data have value for identifying zones of highest risk for in-situ monitoring or the installation of early-warning systems (Cook et al., 2021).

Feature-tracking, DEM difference, and InSAR datasets can be processed and analyzed on a regional or even global scale –
510 and in many cases pre-processed datasets are already available online (e.g. Morin et al., 2016; Gardner et al., 2018)(e.g. Morin et al., 2016; . While these pre-processed datasets are not generally produced for slope stability monitoring, they can be used to improve

hazard maps and reduce landslide related damage. Future advances in Earth observation satellite capabilities and processing algorithms will improve the quality of such products.

5 Conclusions

515 The deadly 7 February 2021 Chamoli rock-ice avalanche was initiated by ~~failure-of~~ the failure of more than 25 Mm³ of
rock and ice high in the Uttarakhand Himalaya. We investigated the conditions of the avalanche source zone over the decades
preceding collapse through a combination of optical and radar satellite images. We used feature tracking to calculate horizontal
slope displacements, and differenced photogrammetrically generated DEMs to investigate vertical displacements. We showed
that the collapsed block moved 20-30 m prior to its collapse, with most rapid motion occurring around 3 years prior to failure.
520 Comparison between our datasets and ~~synthetic-modeled~~ displacement maps shows that the motion occurred primarily via
down-slope translation, opening up a deep crack at the headwall. A combination of permafrost degradation and snow and ice
debris loading within this headwall crack may explain both the lag between initial instability and collapse, and the mid-winter
timing of the collapse. Finally, we assessed the potential of these datasets and approaches for monitoring other unstable slopes.
While they ~~were~~ are effective at identifying precursory signals at a known collapse site, it remains very challenging to predict
525 such collapses with sufficient levels of confidence in high-mountain areas.

Code and data availability. All code used in this study is openly available online. GIV can be downloaded from <https://github.com/MaxVWDV/glacier-image-velocimetry>, AutoRIFT from <https://github.com/nasa-jpl/autoRIFT>, ASP from <https://github.com/NeoGeographyToolkit/StereoPipeline>, and ISCE from <https://github.com/isce-framework/isce2>. The 2015 pre-event DEM is available at <https://doi.org/10.5281/zenodo.4554646>, and the 2021 post-event DEM at <https://doi.org/10.5281/zenodo.4558691>.

530 Appendix A: Pre-event DEM mosaics

A1 CartoSat-1 (2017/2018)

We procured four CartoSat-1 stereo pairs from October 2017 and November 2018 (Supplementary Data sheet) to compute
DEM for an intermediate period between 2015 to 2021. Initial assessments of the CartoSat-1 products revealed high stereo
ray intersection errors (> 100 m) and offsets from reference elevation models (~ 400 m), indicative of poor relative and
535 absolute accuracy of the vendor supplied RPC models. To address these issues we employed ASP's bundle_adjust utility
on all the eight overlapping images and the corresponding RPC models using similar techniques as described in Bhushan
et al. (2021); Dehecq et al. (2020). The bundle adjustment procedure matches similar features between all input overlapping
images and minimises their reprojection error by updating the RPC camera with translation and rotation parameters. Using the
updated RPC model obtained after bundle adjustment, we generated a draft DEM from one of the four pairs using the default
540 ASP settings and aligned it to a filtered and masked version of the HMA 8 m DEM mosaic v2 (Shean, 2021). The alignment

matrix was used to further update the self-consistent RPC model output from bundle adjustment, ensuring improved absolute geolocation accuracy. Following this, the input images were orthorectified at their native resolution of 2.5 m using the 30 m Copernicus DEM (converted to ellipsoidal heights) and stereo processing (correlation and triangulation) was performed for all the four input pairs using the settings described in Shean and Bhushan (2021).

545 The CartoSat-1 DEMs were posted at 10 m resolution with UTM 44N projection and heights above the WGS84 ellipsoid. Consequently, the DEMs were co-registered to the HMA 8 m DEM mosaic v2 (Shean, 2021) over non-glacierized surfaces using a two step procedure: ASP's pc_align followed by Nuth and Kääb (2011) alignment implemented in Shean et al. (2019) to remove any residual horizontal and vertical offsets in the final output DEMs.

A2 SPOT-7 (2018)

550 We also derived a DEM from the December 24, 2018 SPOT-7 stereo pair using ASP's Semi Global Matching correlator and other settings similar to those described in Lacroix (2016); Deschamps-Berger et al. (2020). The final output DEM was posted at a resolution of 10 m with UTM 44N projection and heights above the WGS84 ellipsoid. The DEM was co-registered to the HMA 8 m DEM mosaic v2 (Shean, 2021) over non-glacierized surfaces to ensure consistency with all the DEM products derived in this study.

555 Appendix B: Factor of safety calculations for the Chamoli bloc

The factor of safety FS is calculated from the balance driving and resistive forces (e.g. Záruba and Mencl, 2014; Das and Sivakugan, 2016):

$$FS = \frac{F_R}{F_D} = \frac{AC + Mg\cos(\alpha)\tan(\phi)}{Mg\sin(\alpha)} \quad (\text{B1})$$

In which A is slip surface area, C is cohesion, M is the mass of the unstable region, g is gravity, α is slope, and ϕ is the friction angle. A system may be considered unstable when the factor of safety falls below 1.

Introducing an additional horizontal force F_H modifies this balance in two ways: firstly by increasing the driving force, and secondly by altering the angle between the driving force vector and resistive forces vector:

$$FS = \frac{AC + Mg\cos(\alpha + \alpha')\tan(\phi)}{F_H + Mg\sin(\alpha + \alpha')} \quad (\text{B2})$$

The change in angle of the driving force vector α' is then given by $\alpha' = \arctan(\frac{F_H}{Mg\sin(\alpha)})$. In our situation, for a given mass accumulated in the headwall crack M_C we have $F_H = M_C\sin(\alpha)$.

565 The pre-event storm brought 8.5 to 48 mm water equivalent of precipitation (Shugar et al. (2021); estimates from local weather stations and Weather Research and Forecasting Model). We may use this data to calculate possible loading of this snow on the collapsed block - considering a 500 m long, 70 m wide crack with a 500 m long and fed by a 180 m wide

avalanche zone. Assuming that all of the snowfall was channeled into the crack, total loading M_C would be equal to:

$$570 \quad M_C = A_A * P * \rho_P * g \quad (B3)$$

With A_A being the accumulation area feeding the crack, P being precipitation (in metres), ρ_P being the density of the precipitation. Total snow loading in the headwall crack associated with this single precipitation event would therefore be 10000-60000 kN, equivalent to a slope-parallel horizontal force of 7000-40000 kN.

575 GPM IMGERG precipitation data suggests that around 9 ± 2 m of precipitation fell in the collapse area between crack initiation in 2016 and collapse in 2021. Using the same calculation, maximum snow load in the headwall crack is equal to $8.6-13.5 \times 10^9$ N, equivalent to a slope-parallel horizontal force of $6.3-9.9 \times 10^9$ N. For reference, the estimated total driving force of the collapse bloc, composed of 21 Mm³ of rock and 6 Mm³ of ice, is $\approx 4.0 \times 10^{11}$ N.

Author contributions. All authors designed the study and conducted the research. MVWDV wrote the paper, with input from all co-authors. The final version has been approved by all co-authors.

580 *Competing interests.* The authors declare no competing interests.

Acknowledgements. MVWDV was funded by a University of Minnesota College of Science and Engineering fellowship and a Doctoral Dissertation Fellowship. DHS was funded by Natural Sciences and Engineering Research Council of Canada (NSERC) Discovery Grant 2020-04207. SG and EB acknowledge funding from the French Space Agency (CNES). SG received funding from the Programme National de Télédétection Spatiale (PNTS grant no. PNTS-2018-4). AK acknowledges support from the ESA Glacier CCI project (grant no. 585 4000109873/14/I-NB). MJ was funded by the WSL research program Climate Change Impacts on Alpine Mass Movements (CCAMM) and the Swiss National Science Foundation (grant no. 200021_184634). SB was supported by a NASA FINESST award (80NSSC19K1338). DES was supported by a NASA HiMAT-2 award (80NSSC20K1595). [We acknowledge comments from editor Filippo Catani and two anonymous reviewers, which helped improve this manuscript.](#)

References

- 590 Allen, S. K., Cox, S. C., and Owens, I. F.: Rock avalanches and other landslides in the central Southern Alps of New Zealand: a regional study considering possible climate change impacts, *Landslides*, 8, 33–48, <https://doi.org/10.1007/s10346-010-0222-z>, company: Springer Distributor: Springer Institution: Springer Label: Springer Number: 1 Publisher: Springer-Verlag, 2011.
- Aryal, A., Brooks, B. A., Reid, M. E., Bawden, G. W., and Pawlak, G. R.: Displacement fields from point cloud data: Application of particle imaging velocimetry to landslide geodesy, *Journal of Geophysical Research: Earth Surface*, 117, <https://doi.org/10.1029/2011JF002161>,
595 _eprint: <https://onlinelibrary.wiley.com/doi/pdf/10.1029/2011JF002161>, 2012.
- Barba-Sevilla, M., Baird, B. W., Liel, A. B., and Tiampo, K. F.: Hazard Implications of the 2016 Mw 5.0 Cushing, OK Earthquake from a Joint Analysis of Damage and InSAR Data, *Remote Sensing*, 10, 1715, <https://doi.org/10.3390/rs10111715>, 2018.
- Behling, R., Roessner, S., Kaufmann, H., and Kleinschmit, B.: Automated Spatiotemporal Landslide Mapping over Large Areas Using RapidEye Time Series Data, *Remote Sensing*, 6, 8026–8055, <https://doi.org/10.3390/rs6098026>, 2014.
- 600 Bekaert, D. P. S., Handwerger, A. L., Agram, P., and Kirschbaum, D. B.: InSAR-Based Detection Method for Mapping and Monitoring Slow-Moving Landslides in Remote Regions with Steep and Mountainous Terrain: An Application to Nepal, *Remote Sensing of Environment*, 249, 111983, <https://doi.org/10.1016/j.rse.2020.111983>, 2020.
- Berthier, E., Cabot, V., Vincent, C., and Six, D.: Decadal Region-Wide and Glacier-Wide Mass Balances Derived from Multi-Temporal ASTER Satellite Digital Elevation Models. Validation over the Mont-Blanc Area, *Frontiers in Earth Science*, 4, 63,
605 <https://doi.org/10.3389/feart.2016.00063>, 2016.
- Beyer, R. A., Alexandrov, O., and McMichael, S.: The Ames Stereo Pipeline: NASA’s Open Source Software for Deriving and Processing Terrain Data, *Earth and Space Science*, 5, 537–548, <https://doi.org/10.1029/2018EA000409>, _eprint: <https://onlinelibrary.wiley.com/doi/pdf/10.1029/2018EA000409>, 2018.
- Bhushan, S. and Shean, D.: Chamoli Disaster Pre-event 2-m DEM Composite: September 2015, <https://doi.org/10.5281/zenodo.4554647>,
610 type: dataset, 2021.
- Bhushan, S., Shean, D., Alexandrov, O., and Henderson, S.: Automated digital elevation model (DEM) generation from very-high-resolution Planet SkySat triplet stereo and video imagery, *ISPRS Journal of Photogrammetry and Remote Sensing*, 173, 151–165, <https://doi.org/10.1016/j.isprsjprs.2020.12.012>, 2021.
- Bindschadler, R. A. and Scambos, T. A.: Satellite-Image-Derived Velocity Field of an Antarctic Ice Stream, *Science*, 252, 242–246,
615 <https://doi.org/10.1126/science.252.5003.242>, 1991.
- Bisson, M., Spinetti, C., Andronico, D., Palaseanu-Lovejoy, M., Fabrizia Buongiorno, M., Alexandrov, O., and Cecere, T.: Ten years of volcanic activity at Mt Etna: High-resolution mapping and accurate quantification of the morphological changes by Pleiades and Lidar data, *International Journal of Applied Earth Observation and Geoinformation*, 102, 102369, <https://doi.org/10.1016/j.jag.2021.102369>, 2021.
- 620 Brun, F., Berthier, E., Wagnon, P., Käab, A., and Treichler, D.: A spatially resolved estimate of High Mountain Asia glacier mass balances from 2000 to 2016, *Nature Geoscience*, 10, 668–673, <https://doi.org/10.1038/ngeo2999>, bandiera_abtest: a Cg_type: Nature Research Journals Number: 9 Primary_atype: Research Publisher: Nature Publishing Group Subject_term: Cryospheric science;Hydrology;Projection and prediction Subject_term_id: cryospheric-science;hydrology;projection-and-prediction, 2017.
- Chen, C. and Zebker, H.: Phase unwrapping for large SAR interferograms: statistical segmentation and generalized network models, *IEEE Transactions on Geoscience and Remote Sensing*, 40, 1709–1719, <https://doi.org/10.1109/TGRS.2002.802453>, 2002.
625

- Coe, J. A., Bessette-Kirton, E. K., and Geertsema, M.: Increasing rock-avalanche size and mobility in Glacier Bay National Park and Preserve, Alaska detected from 1984 to 2016 Landsat imagery, *Landslides*, 15, 393–407, <https://doi.org/10.1007/s10346-017-0879-7>, 2018.
- Cook, K. L., Rekapalli, R., Dietze, M., Pilz, M., Cesca, S., Rao, N. P., Srinagesh, D., Paul, H., Metz, M., Mandal, P., Suresh, G., Cotton, F., Tiwari, V. M., and Hovius, N.: Detection and potential early warning of catastrophic flow events with regional seismic networks, *Science*, 630 374, 87–92, <https://doi.org/10.1126/science.abj1227>, publisher: American Association for the Advancement of Science, 2021.
- Corsa, B. D., Jacquemart, M., Willis, M. J., and Tiampo, K. F.: Characterization of large tsunamigenic landslides and their effects using digital surface models: A case study from Taan Fiord, Alaska, *Remote Sensing of Environment*, 270, 112 881, <https://doi.org/10.1016/j.rse.2021.112881>, 2022.
- Crosetto, M., Solari, L., Mróz, M., Balasis-Levinsen, J., Casagli, N., Frei, M., Oyen, A., Moldestad, D. A., Bateson, L., Guerrieri, L., Comerci, V., and Andersen, H. S.: The Evolution of Wide-Area DInSAR: From Regional and National Services to the European Ground Motion Service, *Remote Sensing*, 12, 2043, <https://doi.org/10.3390/rs12122043>, number: 12 Publisher: Multidisciplinary Digital Publishing Institute, 2020.
- Cummins, P. R.: Irrigation and the Palu landslides, *Nature Geoscience*, 12, 881–882, <https://doi.org/10.1038/s41561-019-0467-7>, bandiera_abtest: a Cg_type: Nature Research Journals Number: 11 Primary_atype: News & Views Publisher: Nature Publishing Group Subject_term: Developing world;Hydrogeology;Natural hazards;Tectonics Subject_term_id: developing-world;hydrogeology;natural-hazards;tectonics, 2019.
- Dai, C., Higman, B., Lynett, P. J., Jacquemart, M., Howat, I. M., Liljedahl, A. K., Dufresne, A., Freymueller, J. T., Geertsema, M., Jones, M. W., and Haeussler, P. J.: Detection and Assessment of a Large and Potentially Tsunamigenic Periglacial Landslide in Barry Arm, Alaska, *Geophysical Research Letters*, 47, e2020GL089 800, <https://doi.org/https://doi.org/10.1029/2020GL089800>, _eprint: 645 <https://onlinelibrary.wiley.com/doi/pdf/10.1029/2020GL089800>, 2020a.
- Dai, C., Higman, B., Lynett, P. J., Jacquemart, M., Howat, I. M., Liljedahl, A. K., Dufresne, A., Freymueller, J. T., Geertsema, M., Ward Jones, M., and Haeussler, P. J.: Detection and Assessment of a Large and Potentially-tsunamigenic Periglacial Landslide in Barry Arm, Alaska, *Geophysical Research Letters*, <https://doi.org/10.1029/2020GL089800>, 2020b.
- Dandabathula, G., Sitiraju, S. R., and Jha, C. S.: Investigating the 7th February, 2021 Landslide Triggered Flash Flood in the Himalayan Region Using Geospatial Techniques, *European Journal of Environment and Earth Sciences*, 2, 75–86, <https://doi.org/10.24018/ejgeo.2021.2.4.170>, number: 4, 2021.
- Darvishi, M., Schlögel, R., Bruzzone, L., and Cuozzo, G.: Integration of PSI, MAI, and Intensity-Based Sub-Pixel Offset Tracking Results for Landslide Monitoring with X-Band Corner Reflectors—Italian Alps (Corvara), *Remote Sensing*, 10, 409, <https://doi.org/10.3390/rs10030409>, number: 3 Publisher: Multidisciplinary Digital Publishing Institute, 2018.
- 655 Das, B. M. and Sivakugan, N.: *Fundamentals of geotechnical engineering*, Cengage Learning, 2016.
- Dehecq, A., Gardner, A. S., Alexandrov, O., McMichael, S., Hugonnet, R., Shean, D., and Marty, M.: Automated Processing of Declassified KH-9 Hexagon Satellite Images for Global Elevation Change Analysis Since the 1970s, *Frontiers in Earth Science*, 8, 566 802, <https://doi.org/10.3389/feart.2020.566802>, 2020.
- Deline, P., Gruber, S., Amann, F., Bodin, X., Delaloye, R., Failletaz, J., Fischer, L., Geertsema, M., Giardino, M., Hasler, A., Kirkbride, M., Krautblatter, M., Magnin, F., McColl, S., Ravanel, L., Schoeneich, P., and Weber, S.: Chapter 15 - Ice Loss from Glaciers and Permafrost and Related Slope Instability in High-Mountain Regions, in: *Snow and Ice-Related Hazards, Risks, and Disasters (Second Edition)*, edited by Haeberli, W. and Whiteman, C., pp. 501–540, Elsevier, <https://doi.org/10.1016/B978-0-12-817129-5.00015-9>, 2021.
- 660

- Deschamps-Berger, C., Gascoïn, S., Berthier, E., Deems, J., Gutmann, E., Dehecq, A., Shean, D., and Dumont, M.: Snow depth mapping from stereo satellite imagery in mountainous terrain: evaluation using airborne laser-scanning data, *The Cryosphere*, 14, 2925–2940, <https://doi.org/10.5194/tc-14-2925-2020>, number: 9, 2020.
- 665 Dille, A., Kervyn, F., Handwerger, A. L., d'Oreye, N., Derauw, D., Mugaruka Bibentyo, T., Samsonov, S., Malet, J.-P., Kervyn, M., and Dewitte, O.: When image correlation is needed: Unravelling the complex dynamics of a slow-moving landslide in the tropics with dense radar and optical time series, *Remote Sensing of Environment*, 258, 112 402, <https://doi.org/10.1016/j.rse.2021.112402>, 2021.
- Dimri, A. P., Bookhagen, B., Stoffel, M., and Yasunari, T.: *Himalayan Weather and Climate and their Impact on the Environment*, Springer Nature, google-Books-ID: 7Ea9DwAAQBAJ, 2019.
- 670 Faillettaz, J., Pralong, A., Funk, M., and Deichmann, N.: Evidence of log-periodic oscillations and increasing icequake activity during the breaking-off of large ice masses, *Journal of Glaciology*, 54, 725–737, <https://doi.org/10.3189/002214308786570845>, publisher: Cambridge University Press, 2008.
- Federico, A., Popescu, M., Elia, G., Fidelibus, C., Internò, G., and Murianni, A.: Prediction of Time to Slope Failure: A General Framework, *Environmental Earth Sciences*, 66, 245–256, <https://doi.org/10.1007/s12665-011-1231-5>, 2012.
- 675 Fischer, L., Kääh, A., Huggel, C., and Noetzli, J.: Geology, glacier retreat and permafrost degradation as controlling factors of slope instabilities in a high-mountain rock wall: the Monte Rosa east face, *Natural Hazards and Earth System Sciences*, 6, 761–772, <https://doi.org/10.5194/nhess-6-761-2006>, number: 5 Publisher: Copernicus, 2006.
- Fischer, L., Purves, R. S., Huggel, C., Noetzli, J., and Haeberli, W.: On the influence of topographic, geological and cryospheric factors on rock avalanches and rockfalls in high-mountain areas, *Natural Hazards and Earth System Sciences*, 12, 241–254, <https://doi.org/10.5194/nhess-12-241-2012>, publisher: Copernicus GmbH, 2012.
- 680 Froude, M. J. and Petley, D. N.: Global fatal landslide occurrence from 2004 to 2016, *Natural Hazards and Earth System Sciences*, 18, 2161–2181, <https://doi.org/10.5194/nhess-18-2161-2018>, publisher: Copernicus GmbH, 2018.
- Fukuzono, T.: A Method to Predict the Time of Slope Failure Caused by Rainfall Using the Inverse Number of Velocity of Surface Displacement, *Landslides*, 22, 8–13_1, https://doi.org/10.3313/jls1964.22.2_8, 1985.
- 685 Gardner, A. S., Moholdt, G., Scambos, T., Fahnestock, M., Ligtenberg, S., Broeke, M. v. d., and Nilsson, J.: Increased West Antarctic and unchanged East Antarctic ice discharge over the last 7 years, *The Cryosphere*, 12, 521–547, <https://doi.org/https://doi.org/10.5194/tc-12-521-2018>, publisher: Copernicus GmbH, 2018.
- Geertsema, M., Menounos, B., Bullard, G., Carrivick, J. L., Clague, J. J., Dai, C., Donati, D., Ekstrom, G., Jackson, J. M., Lynett, P., Pichierri, M., Pon, A., Shugar, D. H., Stead, D., Del Bel Belluz, J., Friele, P., Giesbrecht, I., Heathfield, D., Millard, T., Nasonova, S., Schaeffer, A. J., Ward, B. C., Blaney, D., Blaney, E., Brillon, C., Bunn, C., Floyd, W., Higman, B., Hughes, K. E., McInnes, W., Mukherjee, K., and Sharp, M. A.: The 28 November 2020 Landslide, Tsunami, and Outburst Flood – A Hazard Cascade Associated With Rapid Deglaciation at Elliot Creek, British Columbia, Canada, *Geophysical Research Letters*, 49, e2021GL096 716, <https://doi.org/10.1029/2021GL096716>, [_eprint: https://onlinelibrary.wiley.com/doi/pdf/10.1029/2021GL096716](https://onlinelibrary.wiley.com/doi/pdf/10.1029/2021GL096716), 2022.
- 690 Glueer, F., Loew, S., and Manconi, A.: Paraglacial history and structure of the Moosfluh Landslide (1850–2016), Switzerland, *Geomorphology*, 355, 106 677, <https://doi.org/10.1016/j.geomorph.2019.02.021>, 2020.
- Gruber, S. and Haeberli, W.: Permafrost in steep bedrock slopes and its temperature-related destabilization following climate change, *Journal of Geophysical Research: Earth Surface*, 112, <https://doi.org/10.1029/2006JF000547>, publisher: John Wiley & Sons, Ltd, 2007.
- Haeberli, W., Schaub, Y., and Huggel, C.: Increasing risks related to landslides from degrading permafrost into new lakes in de-glaciating mountain ranges, *Geomorphology*, 293, 405–417, <https://doi.org/10.1016/j.geomorph.2016.02.009>, 2017.
- 700

- Handwerger, A. L., Huang, M.-H., Fielding, E. J., Booth, A. M., and Bürgmann, R.: A Shift from Drought to Extreme Rainfall Drives a Stable Landslide to Catastrophic Failure, *Scientific Reports*, 9, 1569, <https://doi.org/10.1038/s41598-018-38300-0>, 2019.
- Heid, T. and Kääh, A.: Evaluation of existing image matching methods for deriving glacier surface displacements globally from optical satellite imagery, *Remote Sensing of Environment*, 118, 339–355, <https://doi.org/10.1016/j.rse.2011.11.024>, 2012.
- 705 Higman, B., Shugar, D. H., Stark, C. P., Ekström, G., Koppes, M. N., Lynett, P., Dufresne, A., Haeussler, P. J., Geertsema, M., Gulick, S., Mattox, A., Venditti, J. G., Walton, M. A. L., McCall, N., Mckittrick, E., MacInnes, B., Bilderback, E. L., Tang, H., Willis, M. J., Richmond, B., Reece, R. S., Larsen, C., Olson, B., Capra, J., Ayca, A., Bloom, C., Williams, H., Bonno, D., Weiss, R., Keen, A., Skanavis, V., and Loso, M.: The 2015 landslide and tsunami in Taan Fiord, Alaska, *Scientific Reports*, 8, 12993, <https://doi.org/10.1038/s41598-018-30475-w>, number: 1 Publisher: Nature Publishing Group, 2018.
- 710 Holm, K., Bovis, M., and Jakob, M.: The landslide response of alpine basins to post-Little Ice Age glacial thinning and retreat in southwestern British Columbia, *Geomorphology*, 57, 201–216, [https://doi.org/10.1016/S0169-555X\(03\)00103-X](https://doi.org/10.1016/S0169-555X(03)00103-X), 2004.
- Howat, I. M., Porter, C., Smith, B. E., Noh, M.-J., and Morin, P.: The Reference Elevation Model of Antarctica, *The Cryosphere*, 13, 665–674, <https://doi.org/https://doi.org/10.5194/tc-13-665-2019>, publisher: Copernicus GmbH, 2019.
- Huggel, C., Clague, J. J., and Korup, O.: Is climate change responsible for changing landslide activity in high mountains?, *Earth Surface Processes and Landforms*, 37, 77–91, <https://doi.org/10.1002/esp.2223>, _eprint: <https://onlinelibrary.wiley.com/doi/pdf/10.1002/esp.2223>, 2012.
- 715 Hugonnet, R., McNabb, R., Berthier, E., Menounos, B., Nuth, C., Girod, L., Farinotti, D., Huss, M., Dussaillant, I., Brun, F., and Kääh, A.: Accelerated global glacier mass loss in the early twenty-first century, *Nature*, 592, 726–731, <https://doi.org/10.1038/s41586-021-03436-z>, number: 7856 Publisher: Nature Publishing Group, 2021.
- 720 Intrieri, E., Carlà, T., and Gigli, G.: Forecasting the Time of Failure of Landslides at Slope-Scale: A Literature Review, *Earth-Science Reviews*, 193, 333–349, <https://doi.org/10.1016/j.earscirev.2019.03.019>, 2019.
- Jacquemart, M. and Tiampo, K.: Leveraging Time Series Analysis of Radar Coherence and Normalized Difference Vegetation Index Ratios to Characterize Pre-Failure Activity of the Mud Creek Landslide, California, *Natural Hazards and Earth System Sciences*, 21, 629–642, <https://doi.org/10.5194/nhess-21-629-2021>, 2021.
- 725 Jacquemart, M., Loso, M., Leopold, M., Welty, E., Berthier, E., Hansen, J. S., Sykes, J., and Tiampo, K.: What drives large-scale glacier detachments? Insights from Flat Creek glacier, St. Elias Mountains, Alaska, *Geology*, 48, 703–707, <https://doi.org/10.1130/G47211.1>, 2020.
- Jakob, L., Gourmelen, N., Ewart, M., and Plummer, S.: Spatially and temporally resolved ice loss in High Mountain Asia and the Gulf of Alaska observed by CryoSat-2 swath altimetry between 2010 and 2019, *The Cryosphere*, 15, 1845–1862, [https://doi.org/10.5194/tc-15-](https://doi.org/10.5194/tc-15-1845-2021)
- 730 1845-2021, publisher: Copernicus GmbH, 2021.
- Jia, H., Wang, Y., Ge, D., Deng, Y., and Wang, R.: Improved offset tracking for predisaster deformation monitoring of the 2018 Jinsha River landslide (Tibet, China), *Remote Sensing of Environment*, 247, 111 899, <https://doi.org/10.1016/j.rse.2020.111899>, 2020.
- Kirschbaum, D., Watson, C. S., Rounce, D. R., Shugar, D. H., Kargel, J. S., Haritashya, U. K., Amatya, P., Shean, D., Anderson, E. R., and Jo, M.: The State of Remote Sensing Capabilities of Cascading Hazards Over High Mountain Asia, *Frontiers in Earth Science*, 7, 197, <https://doi.org/10.3389/feart.2019.00197>, 2019.
- 735 Kirschbaum, D., Kapnick, S. B., Stanley, T., and Pascale, S.: Changes in Extreme Precipitation and Landslides Over High Mountain Asia, *Geophysical Research Letters*, 47, e2019GL085347, <https://doi.org/10.1029/2019GL085347>, _eprint: <https://onlinelibrary.wiley.com/doi/pdf/10.1029/2019GL085347>, 2020.

- Korona, J., Berthier, E., Bernard, M., Rémy, F., and Thouvenot, E.: SPIRIT. SPOT 5 stereoscopic survey of Polar Ice: Reference Images and Topographies during the fourth International Polar Year (2007–2009), *ISPRS Journal of Photogrammetry and Remote Sensing*, 64, 204–212, <https://doi.org/10.1016/j.isprsjprs.2008.10.005>, 2009.
- Kos, A., Amann, F., Strozzi, T., Delaloye, R., von Ruetten, J., and Springman, S.: Contemporary glacier retreat triggers a rapid landslide response, Great Aletsch Glacier, Switzerland, *Geophysical Research Letters*, 43, 12,466–12,474, <https://doi.org/10.1002/2016GL071708>, [eprint: https://onlinelibrary.wiley.com/doi/pdf/10.1002/2016GL071708](https://onlinelibrary.wiley.com/doi/pdf/10.1002/2016GL071708), 2016.
- Krautblatter, M., Funk, D., and Günzel, F. K.: Why permafrost rocks become unstable: a rock–ice–mechanical model in time and space, *Earth Surface Processes and Landforms*, 38, 876–887, <https://doi.org/10.1002/esp.3374>, publisher: John Wiley & Sons, Ltd, 2013.
- Kropáček, J., Vilímek, V., and Mehrishi, P.: A preliminary assessment of the Chamoli rock and ice avalanche in the Indian Himalayas by remote sensing, *Landslides*, 18, 3489–3497, <https://doi.org/10.1007/s10346-021-01742-1>, 2021.
- Kääb, A., Berthier, E., Nuth, C., Gardelle, J., and Arnaud, Y.: Contrasting patterns of early twenty-first-century glacier mass change in the Himalayas, *Nature*, 488, 495–498, <https://doi.org/10.1038/nature11324>, bandiera_abtest: a Cg_type: Nature Research Journals Number: 7412 Primary_atype: Research Publisher: Nature Publishing Group Subject_term: Climate change;Geology Subject_term_id: climate-change;geology, 2012.
- Lacroix, P.: Landslides triggered by the Gorkha earthquake in the Langtang valley, volumes and initiation processes, *Earth, Planets and Space*, 68, 46, <https://doi.org/10.1186/s40623-016-0423-3>, 2016.
- Lacroix, P., Dehecq, A., and Taïpe, E.: Irrigation-triggered landslides in a Peruvian desert caused by modern intensive farming, *Nature Geoscience*, 13, 56–60, <https://doi.org/10.1038/s41561-019-0500-x>, number: 1 Publisher: Nature Publishing Group, 2020.
- Lei, Y., Gardner, A., and Agram, P.: Autonomous Repeat Image Feature Tracking (autoRIFT) and Its Application for Tracking Ice Displacement, *Remote Sensing*, 13, 749, <https://doi.org/10.3390/rs13040749>, number: 4 Publisher: Multidisciplinary Digital Publishing Institute, 2021.
- Leprince, S., Barbot, S., Ayoub, F., and Avouac, J.-P.: Automatic and Precise Orthorectification, Coregistration, and Subpixel Correlation of Satellite Images, Application to Ground Deformation Measurements, *IEEE Transactions on Geoscience and Remote Sensing*, 45, 1529–1558, <https://doi.org/10.1109/TGRS.2006.888937>, 2007.
- Li, H., Haugen, J. E., and Xu, C.-Y.: Precipitation pattern in the Western Himalayas revealed by four datasets, *Hydrology and Earth System Sciences*, 22, 5097–5110, <https://doi.org/10.5194/hess-22-5097-2018>, publisher: Copernicus GmbH, 2018.
- Lucieer, A., de Jong, S. M., and Turner, D.: Mapping Landslide Displacements Using Structure from Motion (SfM) and Image Correlation of Multi-Temporal UAV Photography, *Progress in Physical Geography: Earth and Environment*, 38, 97–116, <https://doi.org/10.1177/0309133313515293>, 2014.
- Magnin, F., Etzelmüller, B., Westermann, S., Isaksen, K., Hilger, P., and Hermanns, R. L.: Permafrost Distribution in Steep Rock Slopes in Norway: Measurements, Statistical Modelling and Implications for Geomorphological Processes, *Earth Surface Dynamics*, 7, 1019–1040, <https://doi.org/10.5194/esurf-7-1019-2019>, 2019.
- Manconi, A.: How Phase Aliasing Limits Systematic Space-Borne DInSAR Monitoring and Failure Forecast of Alpine Landslides, *Engineering Geology*, 287, 106 094, <https://doi.org/10.1016/j.enggeo.2021.106094>, 2021.
- Manconi, A., Kourkoulis, P., Caduff, R., Strozzi, T., and Loew, S.: Monitoring Surface Deformation over a Failing Rock Slope with the ESA Sentinels: Insights from Moosfluh Instability, Swiss Alps, *Remote Sensing*, 10, 672, <https://doi.org/10.3390/rs10050672>, 2018.
- Mao, W., Wu, L., Singh, R. P., Qi, Y., Xie, B., Liu, Y., Ding, Y., Zhou, Z., and Li, J.: Progressive destabilization and triggering mechanism analysis using multiple data for Chamoli rockslide of 7 February 2021, *Geomatics, Natural Hazards and Risk*, 13, 35–53,

- <https://doi.org/10.1080/19475705.2021.2013960>, publisher: Taylor & Francis _eprint: <https://doi.org/10.1080/19475705.2021.2013960>, 2022.
- 780 Massonnet, D. and Feigl, K. L.: Radar Interferometry and Its Application to Changes in the Earth's Surface, *Reviews of Geophysics*, 36, 441–500, <https://doi.org/10.1029/97RG03139>, 1998.
- Massonnet, D., Rossi, M., Carmona, C., Adragna, F., Peltzer, G., Feigl, K., and Rabaute, T.: The Displacement Field of the Landers Earthquake Mapped by Radar Interferometry, *Nature*, 364, 138–142, <https://doi.org/10.1038/364138a0>, 1993.
- 785 McGrath, D., Webb, R., Shean, D., Bonnell, R., Marshall, H.-P., Painter, T. H., Molotch, N. P., Elder, K., Hiemstra, C., and Brucker, L.: Spatially Extensive Ground-Penetrating Radar Snow Depth Observations During NASA's 2017 SnowEx Campaign: Comparison With In Situ, Airborne, and Satellite Observations, *Water Resources Research*, 55, 10026–10036, <https://doi.org/10.1029/2019WR024907>, number: 11 Publisher: John Wiley & Sons, Ltd, 2019.
- Miles, E. S., Watson, C. S., Brun, F., Berthier, E., Esteves, M., Quincey, D. J., Miles, K. E., Hubbard, B., and Wagnon, P.: Glacial and geomorphic effects of a supraglacial lake drainage and outburst event, Everest region, Nepal Himalaya, *The Cryosphere*, 12, 3891–3905, <https://doi.org/10.5194/tc-12-3891-2018>, publisher: Copernicus GmbH, 2018.
- 790 Millan, R., Mouginot, J., Rabatel, A., Jeong, S., Cusicanqui, D., Derkacheva, A., and Chekki, M.: Mapping Surface Flow Velocity of Glaciers at Regional Scale Using a Multiple Sensors Approach, *Remote Sensing*, 11, 2498, <https://doi.org/10.3390/rs11212498>, number: 21 Publisher: Multidisciplinary Digital Publishing Institute, 2019.
- 795 Mondini, A. C., Guzzetti, F., Chang, K.-T., Monserrat, O., Martha, T. R., and Manconi, A.: Landslide Failures Detection and Mapping Using Synthetic Aperture Radar: Past, Present and Future, *Earth-Science Reviews*, 216, 103574, <https://doi.org/10.1016/j.earscirev.2021.103574>, 2021.
- Morin, P., Porter, C., Cloutier, M., Howat, I., Noh, M.-J., Willis, M., Bates, B., Williamson, C., and Peterman, K.: ArcticDEM; A Publically Available, High Resolution Elevation Model of the Arctic, pp. EPSC2016–8396, <https://ui.adsabs.harvard.edu/abs/2016EGUGA..18.8396M>, conference Name: EGU General Assembly Conference Abstracts ADS Bibcode: 2016EGUGA..18.8396M, 2016.
- 800 Motagh, M., Shamshiri, R., Haghshenas Haghighi, M., Wetzel, H.-U., Akbari, B., Nahavandchi, H., Roessner, S., and Arabi, S.: Quantifying Groundwater Exploitation Induced Subsidence in the Rafsanján Plain, Southeastern Iran, Using InSAR Time-Series and in Situ Measurements, *Engineering Geology*, 218, 134–151, <https://doi.org/10.1016/j.enggeo.2017.01.011>, 2017.
- Nuth, C. and Kääb, A.: Co-registration and bias corrections of satellite elevation data sets for quantifying glacier thickness change, *The Cryosphere*, 5, 271–290, <https://doi.org/10.5194/tc-5-271-2011>, 2011.
- 805 Pandey, P., Chauhan, P., Bhatt, C. M., Thakur, P. K., Kannaujia, S., Dhote, P. R., Roy, A., Kumar, S., Chopra, S., Bhardwaj, A., and Aggrawal, S. P.: Cause and Process Mechanism of Rockslide Triggered Flood Event in Rishiganga and Dhauliganga River Valleys, Chamoli, Uttarakhand, India Using Satellite Remote Sensing and in situ Observations, *Journal of the Indian Society of Remote Sensing*, 49, 1011–1024, <https://doi.org/10.1007/s12524-021-01360-3>, 2021.
- Patton, A. I., Rathburn, S. L., and Capps, D. M.: Landslide response to climate change in permafrost regions, *Geomorphology*, 340, 116–128, <https://doi.org/10.1016/j.geomorph.2019.04.029>, 2019.
- 810 Peppas, M. V., Mills, J. P., Moore, P., Miller, P. E., and Chambers, J. E.: Brief communication: Landslide motion from cross correlation of UAV-derived morphological attributes, *Natural Hazards and Earth System Sciences*, 17, 2143–2150, <https://doi.org/10.5194/nhess-17-2143-2017>, publisher: Copernicus GmbH, 2017.
- Petley, D.: Global patterns of loss of life from landslides, *Geology*, 40, 927–930, <https://doi.org/10.1130/G33217.1>, 2012.

- Porter, C., Morin, P., Howat, I., Noh, M.-J., Bates, B., Peterman, K., Keesey, S., Schlenk, M., Gardiner, J., Tomko, K., Willis, M., Kelleher, C., Cloutier, M., Husby, E., Foga, S., Nakamura, H., Platson, M., Wethington, M., Williamson, C., Bauer, G., Enos, J., Arnold, G., Kramer, W., Becker, P., Doshi, A., D'Souza, C., Cummins, P., Laurier, F., and Bojesen, M.: ArcticDEM, <https://doi.org/10.7910/DVN/OHHUKH>, type: dataset, 2018.
- Provost, F., Michéa, D., Malet, J.-P., Boissier, E., Pointal, E., Stumpf, A., Pacini, F., Doin, M.-P., Lacroix, P., Proy, C., and Bally, P.: Terrain deformation measurements from optical satellite imagery: The MPIC-OPT processing services for geohazards monitoring, *Remote Sensing of Environment*, 274, 112 949, <https://doi.org/10.1016/j.rse.2022.112949>, 2022.
- Pörtner, H.-O., Roberts, D. C., Masson-Delmotte, V., Zhai, P., Tignor, M., Poloczanska, E., and Weyer, N. M.: The ocean and cryosphere in a changing climate, 2019.
- Qi, W., Yang, W., He, X., and Xu, C.: Detecting Chamoli landslide precursors in the southern Himalayas using remote sensing data, *Landslides*, 18, 3449–3456, <https://doi.org/10.1007/s10346-021-01753-y>, 2021.
- Rana, N., Sharma, S., Sundriyal, Y., Kaushik, S., Pradhan, S., Tiwari, G., Khan, F., Sati, S. P., and Juyal, N.: A preliminary assessment of the 7th February 2021 flashflood in lower Dhauli Ganga valley, Central Himalaya, India, *Journal of Earth System Science*, 130, 78, <https://doi.org/10.1007/s12040-021-01608-z>, 2021.
- Rosen, P. A., Hensley, S., Zebker, H. A., Webb, F. H., and Fielding, E. J.: Surface Deformation and Coherence Measurements of Kilauea Volcano, Hawaii, from SIR-C Radar Interferometry, *Journal of Geophysical Research: Planets*, 101, 23 109–23 125, <https://doi.org/10.1029/96JE01459>, 1996.
- Rosen, P. A., Gurrola, E., Sacco, G. F., and Zebker, H.: The InSAR scientific computing environment, in: *EUSAR 2012; 9th European Conference on Synthetic Aperture Radar*, pp. 730–733, 2012.
- Samsonov, S. V. and d'Oreye, N.: Multidimensional Small Baseline Subset (MSBAS) for Two-Dimensional Deformation Analysis: Case Study Mexico City, *Canadian Journal of Remote Sensing*, 43, 318–329, <https://doi.org/10.1080/07038992.2017.1344926>, 2017.
- Sättele, M., Bründl, M., and Straub, D.: Reliability and Effectiveness of Early Warning Systems for Natural Hazards: Concept and Application to Debris Flow Warning, *Reliability Engineering & System Safety*, 142, 192–202, <https://doi.org/10.1016/j.ress.2015.05.003>, 2015.
- Schaefer, J. R., Larsen, J. F., and Unema, J. A.: Digital elevation model (DEM) and shaded relief image of Okmok Caldera, 2010, Tech. Rep. RDF 2011-6, Alaska Division of Geological & Geophysical Surveys, <https://doi.org/10.14509/23223>, 2012.
- Shean, D.: HMA 8-m DEM Mosaic v2: Chamoli Region, <https://doi.org/10.5281/ZENODO.4532391>, type: dataset, 2021.
- Shean, D. and Bhushan, S.: Chamoli Disaster Pre-event DEM (2015-05-07 WorldView-1 Stereo), <https://doi.org/10.5281/ZENODO.4533679>, type: dataset, 2021.
- Shean, D., Bhushan, S., Lilien, D., and Meyer, J.: dshean/demcoreg: Zenodo DOI release, <https://doi.org/10.5281/zenodo.3243481>, 2019.
- Shean, D., Bhushan, S., Berthier, E., Deschamps-Berger, C., Gascoin, S., and Knuth, F.: Chamoli Disaster Post-event 2-m DEM Composite (February 10-11, 2021) and Difference Map, <https://doi.org/10.5281/zenodo.4558692>, type: dataset, 2021.
- Shean, D. E., Alexandrov, O., Moratto, Z. M., Smith, B. E., Joughin, I. R., Porter, C., and Morin, P.: An automated, open-source pipeline for mass production of digital elevation models (DEMs) from very-high-resolution commercial stereo satellite imagery, *ISPRS Journal of Photogrammetry and Remote Sensing*, 116, 101–117, <https://doi.org/10.1016/j.isprsjprs.2016.03.012>, 2016.
- Shean, D. E., Bhushan, S., Montesano, P., Rounce, D. R., Arendt, A., and Osmanoglu, B.: A Systematic, Regional Assessment of High Mountain Asia Glacier Mass Balance, *Frontiers in Earth Science*, 7, 363, <https://doi.org/10.3389/feart.2019.00363>, 2020.

- 850 Shrestha, A., Steiner, J., Nepal, S., Maharjan, S., Jackson, M., Rasul, G., and Bjrcharya, B.: Understanding the Chamoli flood: Cause, process, impacts, and context of rapid infrastructure development, <https://www.icimod.org/article/understanding-the-chamoli-flood-cause-process-impacts-and-context-of-rapid-infrastructure-development/>, 2021.
- Shugar, D. H., Jacquemart, M., Shean, D., Bhushan, S., Upadhyay, K., Sattar, A., Schwanghart, W., McBride, S., de Vries, M. V. W., Mergili, M., Emmer, A., Deschamps-Berger, C., McDonnell, M., Bhabri, R., Allen, S., Berthier, E., Carrivick, J. L., Clague, J. J., Dokukin, M.,
855 Dunning, S. A., Frey, H., Gascoïn, S., Haritashya, U. K., Huggel, C., Käab, A., Kargel, J. S., Kavanaugh, J. L., Lacroix, P., Petley, D., Rupper, S., Azam, M. F., Cook, S. J., Dimri, A. P., Eriksson, M., Farinotti, D., Fiddes, J., Gnyawali, K. R., Harrison, S., Jha, M., Koppes, M., Kumar, A., Leinss, S., Majeed, U., Mal, S., Muhuri, A., Noetzli, J., Paul, F., Rashid, I., Sain, K., Steiner, J., Ugalde, F., Watson, C. S., and Westoby, M. J.: A massive rock and ice avalanche caused the 2021 disaster at Chamoli, Indian Himalaya, *Science*, 373, 300–306, <https://doi.org/10.1126/science.abh4455>, publisher: American Association for the Advancement of Science, 2021.
- 860 Stähli, M., Sättele, M., Huggel, C., McArdeïl, B. W., Lehmann, P., Van Herwijnen, A., Berne, A., Schleiss, M., Ferrari, A., Kos, A., Or, D., and Springman, S. M.: Monitoring and Prediction in Early Warning Systems for Rapid Mass Movements, *Natural Hazards and Earth System Sciences*, 15, 905–917, <https://doi.org/10.5194/nhess-15-905-2015>, 2015.
- Stumpf, A., Malet, J. P., Allemand, P., and Ulrich, P.: Surface reconstruction and landslide displacement measurements with Pléïades satellite images, *ISPRS Journal of Photogrammetry and Remote Sensing*, 95, 1–12, <https://doi.org/10.1016/j.isprsjprs.2014.05.008>, 2014.
- 865 Tiampo, K. F., González, P. J., Samsonov, S., Fernández, J., and Camacho, A.: Principal Component Analysis of MS-BAS DInSAR Time Series from Campi Flegrei, Italy, *Journal of Volcanology and Geothermal Research*, 344, 139–153, <https://doi.org/10.1016/j.jvolgeores.2017.03.004>, 2017.
- Tiwari, A., Sain, K., Kumar, A., Tiwari, J., Paul, A., Kumar, N., Haldar, C., Kumar, S., and Pandey, C. P.: Potential seismic precursors and surficial dynamics of a deadly Himalayan disaster: an early warning approach, *Scientific Reports*, 12, 3733, <https://doi.org/10.1038/s41598-022-07491-y>, number: 1 Publisher: Nature Publishing Group, 2022.
- 870 Uhlemann, S., Smith, A., Chambers, J., Dixon, N., Dijkstra, T., Haslam, E., Meldrum, P., Merritt, A., Gunn, D., and Mackay, J.: Assessment of ground-based monitoring techniques applied to landslide investigations, *Geomorphology*, 253, 438–451, <https://doi.org/10.1016/j.geomorph.2015.10.027>, 2016.
- van Westen, C., van Asch, T., and Soeters, R.: Landslide Hazard and Risk Zonation—Why Is It Still so Difficult?, *Bulletin of Engineering Geology and the Environment*, 65, 167–184, <https://doi.org/10.1007/s10064-005-0023-0>, 2006.
- 875 van Westen, C. J. and Lulie Getahun, F.: Analyzing the evolution of the Tessina landslide using aerial photographs and digital elevation models, *Geomorphology*, 54, 77–89, [https://doi.org/10.1016/S0169-555X\(03\)00057-6](https://doi.org/10.1016/S0169-555X(03)00057-6), number: 1, 2003.
- Van Wyk de Vries, M. and Wickert, A. D.: Glacier Image Velocimetry: an open-source toolbox for easy and rapid calculation of high-resolution glacier velocity fields, *The Cryosphere*, 15, 2115–2132, <https://doi.org/10.5194/tc-15-2115-2021>, publisher: Copernicus GmbH,
880 2021.
- Vincent, C., Thibert, E., Harter, M., Soruco, A., and Gilbert, A.: Volume and frequency of ice avalanches from Tacconnaz hanging glacier, French Alps, *Annals of Glaciology*, 56, 17–25, <https://doi.org/10.3189/2015AoG70A017>, publisher: Cambridge University Press, 2015.
- Wasowski, J. and Bovenga, F.: Investigating Landslides and Unstable Slopes with Satellite Multi Temporal Interferometry: Current Issues and Future Perspectives, *Engineering Geology*, 174, 103–138, <https://doi.org/10.1016/j.enggeo.2014.03.003>, 2014.
- 885 Wegmann, M., Funk, M., Flotron, A., and Keusen, H.: Movement Studies to Forecast the Time of Breaking off of Ice and Rock Masses, in: *Early Warning Systems for Natural Disaster Reduction*, edited by Zschau, J. and Küppers, A., pp. 565–568, Springer Berlin Heidelberg, Berlin, Heidelberg, https://doi.org/10.1007/978-3-642-55903-7_76, 2003.

- Willis, M. J., Zheng, W., Durkin, W. J., Pritchard, M. E., Ramage, J. M., Dowdeswell, J. A., Benham, T. J., Bassford, R. P., Stearns, L. A.,
890 Glazovsky, A. F., Macheret, Y. Y., and Porter, C. C.: Massive destabilization of an Arctic ice cap, *Earth and Planetary Science Letters*,
502, 146–155, <https://doi.org/10.1016/j.epsl.2018.08.049>, 2018.
- Zheng, W., Pritchard, M. E., Willis, M. J., and Stearns, L. A.: The Possible Transition From Glacial Surge to Ice
Stream on Vavilov Ice Cap, *Geophysical Research Letters*, 46, 13 892–13 902, <https://doi.org/10.1029/2019GL084948>, _eprint:
<https://onlinelibrary.wiley.com/doi/pdf/10.1029/2019GL084948>, 2019.
- Zhou, Y., Li, X., Zheng, D., Li, Z., An, B., Wang, Y., Jiang, D., Su, J., and Cao, B.: The joint driving effects of climate and weather
895 changes caused the Chamoli glacier-rock avalanche in the high altitudes of the India Himalaya, *Science China Earth Sciences*,
<https://doi.org/10.1007/s11430-021-9844-0>, 2021.
- Záruba, Q. and Mencl, V.: *Landslides and Their Control*, Elsevier, google-Books-ID: kaw7AAAAQBAJ, 2014.